Research Article
doi.org/10.1002/batt.202200327

Chemistry Europe
European Chemical Societies Publishing

www.batteries-supercaps.org

Survey of Zirconium-Containing NaSICON-type Solid-State Li^+ Ion Conductors with the Aim of Increasing Reduction Stability by Partial Cation Substitution

Asmaa Loutati,*[a, b, c] Philipp Odenwald,[a, c] Burak Aktekin,[d] Joachim Sann,[d] Olivier Guillon,[a, b, e] Frank Tietz,*[a, b] and Dina Fattakhova-Rohlfing[a, b, c]

Various compositions of the series $Li_{1+x}M^{3+}{}_xZr_{2-x}(PO_4)_3$ where $M^{3+} = Al^{3+}$, Sc^{3+}, Y^{3+} were prepared by solution-assisted solid-state reaction, since they could have a higher reduction stability as solid electrolytes in lithium batteries than in germanium- or titanium-containing materials. The influence of substitution on crystallographic parameters, density, and ionic conductivity were investigated. The cation substitution of M^{3+} (M = Al, Sc, Y) for Zr^{4+} in $LiZr_2(PO_4)_3$ stabilizes the rhombohedral NaSICON structure (space group $R\bar{3}c$) at room temperature and increases the ionic conductivity significantly. Here, at 25 °C and with a consistent relative density of 94%–96%, an ionic conductivity of 2.7×10^{-5} S cm^{-1}, 6.7×10^{-5} S cm^{-1}, and 3.6×10^{-6} S cm^{-1} was achieved with the compositions $Li_{1.2}Sc_{0.2}Zr_{1.8}(PO_4)_3$, $Li_{1.2}Y_{0.2}Zr_{1.8}(PO_4)_3$, and $Li_{1.2}Al_{0.2}Zr_{1.8}(PO_4)_3$, respectively. In comparison with $Li_{1+x}Sc_xZr_{2-x}(PO_4)_3$, the Y^{3+} substitution in $LiZr_2(PO_4)_3$ enhanced the ionic conductivity slightly and denoted the maximum Li^+ ionic conductivity obtained at room temperature. However, substitution with Al^{3+} decreased the ionic conductivity. For the first time, this work provides a complete overview of three series of solid Li-ion conductors in the Li_2O-M_2O_3-ZrO_2-P_2O_5 system where M = Al, Sc, Y. Noticeable differences in the chemistry of resulting compounds were observed, which likely depend on the ionic radius of the cations being substituted. The series with Sc showed complete miscibility from $x = 0$ to $x = 2$ with a continuous change of the NaSICON polymorphs. The series with Y showed a solubility limit at about $x = 0.3$ and higher substitution levels led to the increasing formation of YPO_4. The series with Al exhibited continuously decreasing ionic conductivity until $x = 1$, whereupon the investigation was terminated due to its very low conductivity of about 10^{-10} S cm^{-1}.

Introduction

Li-containing NaSICON materials are currently receiving a great deal of attention as solid-state electrolytes in electrochemical energy storage systems due to their high ionic conductivity and high chemical stability in air.[1,2] Within this class of materials, the lithium aluminum germanium phosphates $Li_{1+x}Al_xGe_{2-x}(PO_4)_3$ and lithium aluminum titanium phosphates $Li_{1+x}Al_xTi_{2-x}(PO_4)_3$ are the solid-state Li-ion conductors with the highest ionic conductivity at room temperature.[3] Aono et al.[4] studied the electrical properties of the materials $Li_{1+x}M_xTi_{2-x}P_3O_{12}$ (M = Al, Cr, Ga, Fe, In, La, Sc and Y), recording a maximum total ionic conductivity of 7×10^{-4} S cm^{-1} at room temperature (RT) for $Li_{1.3}Al_{0.3}Ti_{1.7}P_3O_{12}$. Similarly, $Li_{1+x}Al_xGe_{2-x}P_3O_{12}$ materials exhibit very high ionic conductivity at room temperature (RT) within a wide stoichiometry range. Kumar et al. and Fu et al. reported that the materials $Li_{1.5}Al_{0.5}Ge_{1.5}P_3O_{12}$ and $Li_{1.4}Al_{0.4}Ge_{0.6}P_3O_{12}$ have a total ionic conductivity of 10^{-2} S cm^{-1} and 10^{-4} S cm^{-1}, respectively.[5,6] However, the instability of Ti^{4+} and Ge^{4+} against reduction to Ti^{3+} and Ge^{2+} in direct contact with lithium metal as anode still raises many challenges,[7] causing severe performance degradation and restricting the application of NaSICON-type solid-state electrolytes (SSEs) in all-solid-state Li metal batteries (ASS-LMBs).[8,9] Hence, there is still a need to develop Ti/Ge-free NaSICON-type Li^+ ionic conductors with improved thermody-

[a] A. Loutati, P. Odenwald, Prof. Dr. O. Guillon, Dr. F. Tietz, Prof. Dr. D. Fattakhova-Rohlfing
Forschungszentrum Jülich GmbH
Institute of Energy and Climate Research: Materials Synthesis and Processing (IEK-1)
D-52425 Jülich, Germany
E-mail: a.loutati@fz-juelich.de
f.tietz@fz-juelich.de
[b] A. Loutati, Prof. Dr. O. Guillon, Dr. F. Tietz, Prof. Dr. D. Fattakhova-Rohlfing
Forschungszentrum Jülich GmbH
Helmholtz-Institute Münster: Ionics in Energy Storage (IEK-12)
D-52425 Jülich, Germany
[c] A. Loutati, P. Odenwald, Prof. Dr. D. Fattakhova-Rohlfing
Universität Duisburg-Essen
Faculty of Engineering
Lotharstr. 1, 47057 Duisburg, Germany
[d] Dr. B. Aktekin, Dr. J. Sann
Justus Liebig University Gießen
Institute of Physical Chemistry
Heinrich-Buff-Ring. 17, 35392 Gießen, Germany
[e] Prof. Dr. O. Guillon
Jülich Aachen Research Alliance
JARA-Energy, Germany

Supporting information for this article is available on the WWW under https://doi.org/10.1002/batt.202200327

namic stability, although there is a long history of attempts to achieve this. In the present work, the information on Zr-containing NaSICON materials that has been gained during recent decades was compiled and three series were revisited with the aim of exploring and increasing their ionic conductivities with modern processing and sintering techniques.

The ionic conductivity of $LiZr_2(PO_4)_3$ (LZP) was studied numerous times and a wide range of ionic conductivity from 10^{-8} to 10^{-6} S cm^{-1} was observed depending on the preparation method, final lithium stoichiometry, crystallographic symmetry, density, and microstructure of the sintered pellets.[10–15] The ionic conductivity in NaSICON-type materials can be significantly improved by partial substitution of tetravalent metal cations with trivalent ones, resulting in additional lithium ions in the structure and thus improving charge carrier mobility.[1,3–6,16] Furthermore, the incorporation of elements of different ionic sizes into the crystal structure of LZP can adjust the size of bottlenecks of lithium transport pathways and control the ionic conductivity. In this regard, several NaSICON-type materials have already been investigated.[1,11–13,15,17–23]

Mariappan et al. and Li et al.[12,21] stabilized the rhombohedral structure of LZP at RT by substituting Y^{3+} for Zr^{4+}. The authors studied the electrical properties of the compounds $Li_{1+x}Y_xZr_{2-x}(PO_4)_3$ where $0.1 \leq x \leq 0.2$[12] and $0.05 \leq x \leq 0.2$,[21] respectively, and obtained a considerably improved total ionic conductivity of 0.7×10^{-4} S cm^{-1} at 25 °C[21] for $Li_{1.15}Y_{0.15}Zr_{1.85}(PO_4)_3$ densified by spark plasma sintering. The authors reported that Y^{3+} is a suitable substitution ion for Zr^{4+} in LZP, causing an increase of the lattice parameters and cell volume due to the different values of ionic radii of Zr^{4+} (0.72 Å) and Y^{3+} (0.9 Å).[24]

Savitha et al.[23] and Zhang et al.[22] examined the systems $Li_xAlZr(PO_4)_3$ ($x = 1.8$, 2.0, 2.2) and $Li_{1+x}Al_xZr_{2-x}(PO_4)_3$ ($x = 0.2$, 0.225, 0.25, 0.275, 0.3, 0.5), respectively, to obtain an ionic conductivity of 4.4×10^{-5} S cm^{-1} for the sample $Li_{2.2}AlZr(PO_4)_3$ at 400 °C[23] and 3.1×10^{-6} S cm^{-1} for $Li_{1.0.275}Al_{0.275}Zr_{1.725}(PO_4)_3$ at RT.[22] Cassel et al.[20] obtained a stable rhombohedral phase with $Li_{1.2}Ca_{0.1}Zr_{1.9}(PO_4)_3$, which exhibited an enhanced ionic conductivity at RT of 1.2×10^{-7} S cm^{-1} and 7.2×10^{-7} S cm^{-1} for the material prepared by solid-state reaction and by sol-gel synthesis, respectively. Substitution with Sr was also investigated, and the compound $Li_{1.2}Sr_{0.1}Zr_{1.9}(PO_4)_3$ prepared by the sol-gel method achieved the highest ionic conductivity of 3.4×10^{-5} S cm^{-1}.[11] The latter material was also prepared by Smith et al.[18] using classical solid-state reaction synthesis. Here, the total ionic conductivity was 2.1×10^{-5} S cm^{-1} with a relative density of ~97 % after hot pressing.

The ionic conductivity of $Li_3Sc_2(PO_4)_3$ (LSP) was measured at 10^{-7} S cm^{-1}.[24] Amatucci et al. investigated the optimization of LSP by substituting Al^{3+} and Y^{3+} for Sc^{3+}. The ionic conductivities at RT were reported to be 1.5×10^{-5} S cm^{-1}, 5×10^{-6} S cm^{-1} and 5×10^{-5} S cm^{-1} for $Li_3Sc_{1.6}Al_{0.4}(PO_4)_3$, $Li_3Sc_{1.5}Y_{0.5}(PO_4)_3$ and $Li_{4.8}Sc_{1.4}(PO_4)_3$, respectively.[25] Furthermore, $Li_{2.8}Sc_{1.8}Zr_{0.2}(PO_4)_3$ has an ionic conductivity of 2×10^{-6} S cm^{-1}.[24]

Suzuki et al. described the synthesis, structure, and ionic conductivity of Li-ion conductors of $Li_{3+2x}(Sc_{1-x}Mg_x)_2(PO_4)_3$, $Li_{3-4x}(Sc_{1-x}M_x)_2(PO_4)_3$ (M = Nb, Ta),[26] and $Li_{3-2x}(Sc_{1-x}M_x)_2(PO_4)_3$ (M = Ti, Zr, Sn, Hf).[26,27] Ionic conductivity data of the members of these solid solutions are summarized in Table S1 in the supporting information.

Sato et al.[28] studied the system $Li_{3-2x}(Sc_{1-x}Zr_x)_2(PO_4)_3$. The best reported value of ionic conductivity was 1.04×10^{-3} S cm^{-1} at 150 °C for the sample with $x = 0.05$, but no value was reported for ambient temperature.

The research results of the partial cation substitutions show improvements in ionic conductivity, but the values still do not meet the requirements for high battery performance. Moreover, the results confirmed that most crystal structures for NaSICON materials have rhombohedral symmetry with space group $R\bar{3}c$. Orthorhombic, monoclinic, and triclinic symmetry variations appear less frequently, depending on composition, synthesis conditions, and temperature. On the one hand, high sintering temperatures stabilize the rhombohedral phase linked with fast Li^+ ion conductivity. On the other hand, sintering at high temperatures increases the evaporation of lithium species and the occurrence of micro-cracks during cooling from high temperature to RT. Therefore, stabilizing the rhombohedral symmetry of the material at low sintering temperatures and short dwell times is key to avoiding micro-cracks, limiting lithium evaporation, and achieving high relative density and high ionic conductivity. To this end, in this study, the $Li_{1+x}M^{3+}{}_xZr_{2-x}(SiO_4)_y(PO_4)_{3-y}$ system where $M^{3+} = Al^{3+}$, Sc^{3+}, Y^{3+} is re-examined through the systematic optimization of sintering conditions to further increase the ionic conductivity of NaSICON materials. In addition, this work will provide a broader insight into the properties of NaSICON materials substituted with trivalent ions. In Figure 1, the materials presented in this work correspond to the horizontally arranged green spheres ($y = 0$). In a separate publication, we will discuss the materials with substitutions in the polyanionic sublattice, i.e., the vertically arranged green spheres (with $M^{3+} = Sc^{3+}$). The thermal, crystallographic, microstructural, and electrical proper-

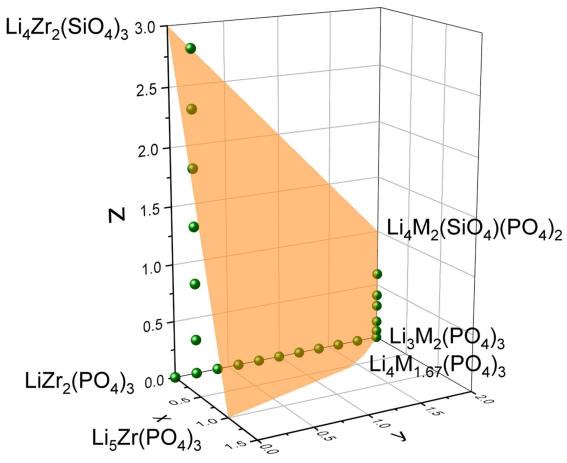

Figure 1. Exploratory research of NaSICON materials in the Li_2O-M_2O_3-ZrO_2-SiO_2-P_2O_5 system. The orange surface corresponds to the compositional limits of the NaSICON materials. The green spheres denote the investigated samples. In this work, only the horizontally arranged spheres are discussed.

Research Article
doi.org/10.1002/batt.202200327
Chemistry Europe
European Chemical Societies Publishing

ties of the prepared samples are evaluated and discussed in comparison with previously obtained results.

Results and Discussion

Scandium substitutions: $Li_{1+x}Sc_xZr_{2-x}(PO_4)_3$ ($0 \le x \le 2$)

For the investigation of the $Li_{1+x}Sc_xZr_{2-x}(PO_4)_3$ series, the substitution of zirconium with scandium was varied from $x=0$ to $x=2$ with intervals of 0.2. To obtain the optimum sintering condition for each material and dense ceramics of a high quality, the shrinkage behavior of the pellets was characterized by dilatometry (see Figures S1a and 14a for the material where $x=0.2$). The shrinkage was recorded during constant heating until a shrinkage of around 23% was reached. The pressed pellets were subsequently sintered in the furnace in air at varying temperatures in 10 °C steps between the temperatures defined by 10% shrinkage (T10%) and 23% shrinkage (T23%) in the corresponding dilatometry curve. After several sintering tests in the same oven applying the same conditions (3 h, 300 K/h cooling and heating), the optimum sintering temperatures offering the highest relative densities were determined and are listed in Tables 1 and 4. No significant shrinkage was obtained below the listed temperatures. Above the listed temperatures, the formation of micro-cracks was observed. For the material where $x=1.6$, the sintering experiments were performed only from 900 °C to 985 °C in 10 °C steps, since the pellets melted at about 1000 °C. For samples where $x=2$, the sintering experiments were also carried out only from 900 °C to 1000 °C. The dilatometry curve showed expansion starting at about 1000 °C, and sintering at higher temperatures also resulted in the expansion of the pellets and a very low density.

Figure 2 shows the XRD patterns of $Li_{1+x}Sc_xZr_{2-x}(PO_4)_3$ ($0 \le x \le 2$) after sintering at the temperatures listed in Table 1. The indexing of the reflections in the powder XRD patterns showed that all compositions crystallize with a NaSICON structure. The rhombohedral phase ($R\bar{3}c$; Inorganic Crystal Structure Database (ICSD) no. 191891)[21] was stabilized at RT for the composition where $x=0.2$, similar to the substitutions with Ca or Sr in LZP.[13,18] The diffraction peaks observed for $x=0.2$ were assigned to a pure NaSICON structure without any impurity phase. For compositions where $0.4 \le x \le 1.4$, the XRD patterns show the presence of a mixture of rhombohedral and monoclinic ($P2_1/n$; ICSD no. 91112)[34] symmetry. Moreover, for the mixture of rhombohedral and monoclinic phases, the orthorhombic phase (*Pbcn;* ICSD no. 83913)[28] appeared in compositions where $1.6 \le x \le 2$, which is in good agreement with the previous work by Sato et al. for $Li_{3-2x}Sc_{2-2x}Zr_{2x}(PO_4)_3$.[28] The contents (in wt.%) of the different phases for all $Li_{1+x}Sc_xZr_{2-x}(PO_4)_3$ compositions are listed in Table 2 and presented in Figure 16.

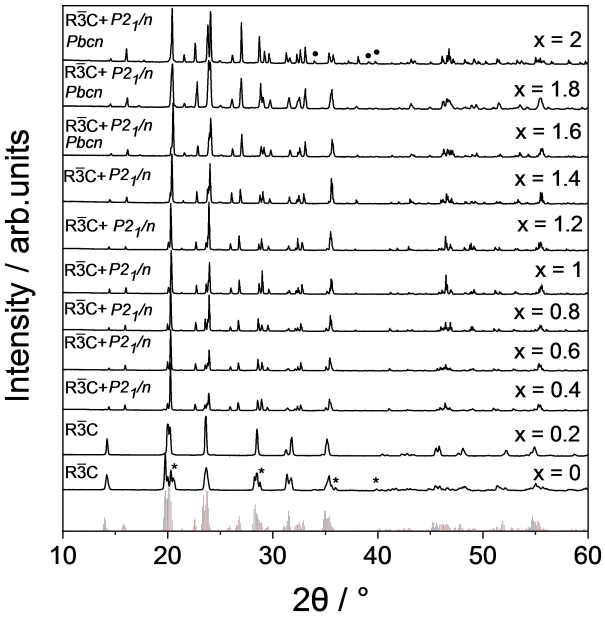

Figure 2. XRD patterns of LSZP where $0 \le x \le 2$ after sintering at optimum conditions (Tables 1 and 4). The reference patterns at the bottom are taken from the Inorganic Crystal Structure Database (ICSD), P21/n; ICSD no. 91112 (blue),[34] Pbcn; ICSD no. 83913 (red),[28] $R\bar{3}c$; ICSD no. 191891 (black).[21] The symbols * and ● indicate $Zr_2O(PO_4)_2$ and Sc_2O_3, respectively.

Table 1. Optimized free sintering temperatures (°C) for $Li_{1+x}M_xZr_{2-x}(PO_4)_3$ where M = Sc, Y, Al. In all cases, a constant dwell time of 3 h was applied at the given temperatures.

x	M = Sc	M = Y	M = Al
0	1300	1300	1300
0.2	1280	1250	1250
0.4	1250	1250	1100
0.6	1250	1250	1050
0.8	1250	1100	1010
1	1200	980	950
1.2	1230	1000	–
1.4	1250	1000	–
1.6	985	980	–
1.8	1150	980	–
2	1000	980	–

A significant amount of $Zr_2O(PO_4)_2$ was detected as an impurity in LZP. The formation of $Zr_2O(PO_4)_2$ during the sintering of $Li_{1+x}Sc_xZr_{2-x}(PO_4)_3$ was also observed by Šalkus et al.[24] Furthermore, in LSP ($x=2$) a small amount of unreacted scandium oxide was found. The amount of orthorhombic $Zr_2O(PO_4)_2$ phase (space group *Cmca;* ICSD no. 1922)[35] was refined as 10 wt.% and that of monoclinic Sc_2O_3 phase (space group *C2/m;* ICSD no. 160218)[36] as 4 wt.% according to Rietveld analysis. In Figure 2, the impurity phase is denoted by an asterisk for $Zr_2O(PO_4)_2$ and by a filled circle for Sc_2O_3.

The lattice parameters and cell volume of $Li_{1+x}Sc_xZr_{2-x}(PO_4)_3$ ($0 \le x \le 2$) obtained by Rietveld refinement and structural literature data of LZP[13] are summarized in Table 2. The refinements were performed on the basis of space groups given in Table 2. For better comparison, the lattice parameters and unit cell volume of rhombohedral (space group $R\bar{3}c$) and orthorhombic (space group *Pbcn*) symmetry were converted to monoclinic symmetry (space group $P2_1/n$). These converted data are summarized in Table S2 in the supporting information.

The evolution of the XRD pattern of $Li_{1.2}Sc_{0.2}Zr_{1.8}(PO_4)_3$ after sintering at different stages of heat treatment is shown in

Research Article
doi.org/10.1002/batt.202200327
Chemistry Europe
European Chemical Societies Publishing

Table 2. Lattice parameters, unit cell volume, space group, and content of NaSICON polymorphs in $Li_{1+x}Sc_xZr_{2-x}(PO_4)_3$ ($0 \le x \le 2$).

x	Material	a [Å]	b [Å]	c [Å]	β [°]	V [Å^3]	Space group	Content [wt.%]
0	$LiZr_2(PO_4)_3$ [13]	8.8600(1)	8.8600(1)	22.065(1)	90	1500.04	$R\bar{3}c$	–
0	$LiZr_2(PO_4)_3$ [*]	8.808(1)	8.808(1)	22.517(3)	90	1512.85	$R\bar{3}c$	90
0.2	$Li_{1.2}Sc_{0.2}Zr_{1.8}(PO_4)_3$	8.864(2)	8.864(2)	22.120(2)	90	1505.13	$R\bar{3}c$	100
0.4	$Li_{1.4}Sc_{0.4}Zr_{1.6}(PO_4)_3$	8.885(1)	8.885(1)	22.057(3)	90	1507.97	$R\bar{3}c$	58
		8.784(2)	8.967(3)	12.430(2)	91.017	978.89	$P2_1/n$	42
0.6	$Li_{1.6}Sc_{0.6}Zr_{1.4}(PO_4)_3$	8.907(3)	8.907(3)	22.057(1)	90	1515.44	$R\bar{3}c$	54
		8.764(2)	8.974(2)	12.447(3)	91.170	978.73	$P2_1/n$	46
0.8	$Li_{1.8}Sc_{0.8}Zr_{1.2}(PO_4)_3$	8.895(1)	8.895(1)	22.057(1)	90	1511.36	$R\bar{3}c$	52
		8.759(3)	8.977(1)	12.434(3)	91.200	977.46	$P2_1/n$	48
1	$Li_2ScZr(PO_4)_3$	8.839(2)	8.839(2)	22.057(2)	90	1492.39	$R\bar{3}c$	50
		8.750(3)	8.868(3)	12.353(1)	89.937	958.53	$P2_1/n$	50
1.2	$Li_{2.2}Sc_{1.2}Zr_{0.8}(PO_4)_3$	8.834(1)	8.834(1)	22.058(3)	90	1490.77	$R\bar{3}c$	49
		8.749(3)	8.885(2)	12.356(1)	89.862	960.49	$P2_1/n$	51
1.4	$Li_{2.4}Sc_{1.4}Zr_{0.6}(PO_4)_3$	8.839(2)	8.839(2)	22.058(3)	90	1492.46	$R\bar{3}c$	42
		8.776(1)	8.861(3)	12.361(2)	90.011	961.24	$P2_1/n$	58
1.6	$Li_{2.6}Sc_{1.6}Zr_{0.4}(PO_4)_3$	8.846(1)	8.846(1)	22.057(1)	90	1494.76	$R\bar{3}c$	32
		8.789(2)	8.845(1)	12.395(3)	90.040	963.57	$P2_1/n$	62
		12.365(1)	8.785(2)	8.854(1)	90	961.8	*Pbcn*	6
1.8	$Li_{2.8}Sc_{1.8}Zr_{0.2}(PO_4)_3$	8.865(3)	8.865(1)	22.058(3)	90	1501.25	$R\bar{3}c$	14
		8.812(3)	8.845(1)	12.375(2)	89.822	964.53	$P2_1/n$	72
		12.371(2)	8.807(1)	8.841(3)	90	963.2	*Pbcn*	14
2	$Li_3Sc_2(PO_4)_3$ [**]	8.809(1)	8.809(1)	22.058(2)	90	1482.35	$R\bar{3}c$	7
		8.816(2)	8.851(1)	12.286(1)	90.083	958.68	$P2_1/n$	73
		12.299(1)	8.856(2)	8.807(1)	90	959.3	*Pbcn*	16

[*]: Contains 10 wt.% $Zr_2O(PO_4)_2$; [**]: contains 4 wt.% Sc_2O_3

Figure 3. A significant change was observed in the patterns upon increasing the sintering temperature. Initially at 900 °C, the reflection at $2\theta = 20.37°$ was sharper than after sintering at 1000 °C, consisting of one intense reflection with a shoulder at $2\theta = 20.04°$. At higher temperatures, the reflection started to increase in intensity and at 1250 °C it became a doublet with the same intensity. Beyond 1250 °C, the two neighboring reflections converged and became a single reflection at 1280 °C. In combination with the vanishing of other reflections, this indicates a phase transition to a higher crystal symmetry. Analysis of XRD patterns from 900 °C to 1200 °C showed that monoclinic symmetry was predominant compared to rhombohedral symmetry. At 1250 °C, the rhombohedral symmetry was dominant, and the Rietveld refinement showed 24 wt.% and 76 wt.% for the monoclinic and rhombohedral phases, respectively. At 1280 °C,

the pure rhombohedral phase was stabilized. Kumar et al.[11] also reported the formation of phase mixture in LZP consisting of triclinic $C\bar{1}$ and rhombohedral $R\bar{3}c$ fractions. This phase mixture differs from the result obtained here. The variation of crystallographic symmetry could be influenced by different factors such as the temperature of the heat treatment and also the use of different starting materials. However, as shown in Figure 3, sintering at 1280 °C can provide the pure rhombohedral NaSICON structure.

In addition, at 900 °C and 1000 °C, the sample contained different amounts of monoclinic ZrP_4O_{12} (space group *C1c1*; ICSD no. 23014)[37] as a secondary phase. However, no impurity was detected at 1200 °C and above.

Rietveld refinement was performed to obtain the lattice parameters, unit cell volume, and crystallographic density (d_x) of $Li_{1.2}Sc_{0.2}Zr_{1.8}(PO_4)_3$ during phase evolution. The results of the refinement are presented in Table 3. The increase in the sintering temperature of the investigated compound leads to a

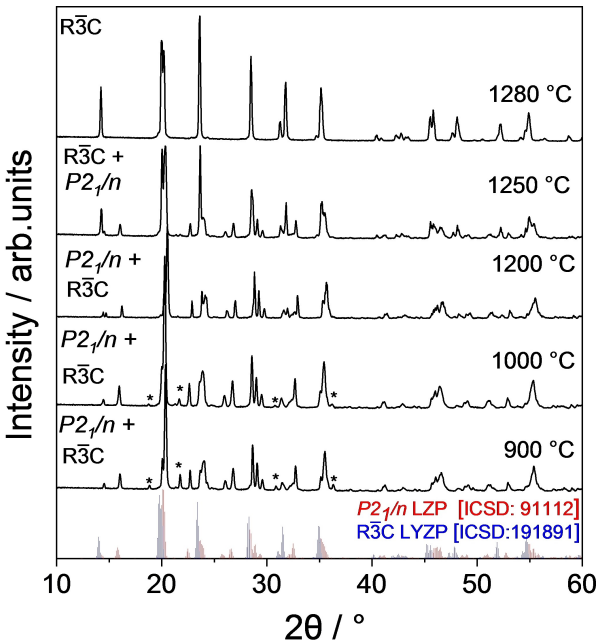

Figure 3. Phase evolution of $Li_{1.2}Sc_{0.2}Zr_{1.8}(PO_4)_3$ after sintering at different temperatures from 900 ° C to 1280 °C. *: ZrP_4O_{12}

Research Article
doi.org/10.1002/batt.202200327
Chemistry Europe
European Chemical Societies Publishing

Table 3. Unit cell parameters and space group of $Li_{1.2}Sc_{0.2}Zr_{1.8}(PO_4)_3$ after sintering at different temperatures.

Temp. [°C]	*a* [Å]	*b* [Å]	*c* [Å]	*β* [°]	*V* [Å^3]	*V*/*Z* [Å^3]	Space group	Density [g/cm^3]
900	8.910(1)	8.910(2)	22.057(1)	90	1516.47	252.7	$R\bar{3}c$	3.26
	8.806(4)	8.934(5)	12.360(3)	89.901(3)	972.40	243.1	$P2_1/n$	
1000	8.877(3)	8.877(1)	22.061(2)	90	1505.53	250.9	$R\bar{3}c$	3.24
	8.816(2)	8.932(1)	12.373(1)	89.907(1)	974.31	243.6	$P2_1/n$	
1200	8.861(1)	8.861(3)	22.065(2)	90	1500.38	250.1	$R\bar{3}c$	3.23
	8.818(2)	8.935(1)	12.373(1)	90.015(2)	974.85	243.7	$P2_1/n$	
1250	8.848(1)	8.848(2)	22.114(1)	90	1499.0	249.8	$R\bar{3}c$	3.23
	8.817(1)	8.935(2)	12.374(1)	90.018(1)	974.82	243.7	$P2_1/n$	
1280	8.864(2)	8.864(2)	22.120(2)	90	1505.13	250.8	$R\bar{3}c$	3.09

small increase of the unit cell volume up to 1250 °C, while the phase transition at 1280 °C leads to a significant expansion of the crystal lattice.

To study the impact of scandium substitution on ionic conductivity for zirconium in $Li_{1+x}Sc_xZr_{2-x}(PO_4)_3$, impedance spectra were measured at 25 °C. The Nyquist plots of the spectra are shown in Figure 4. A single semicircle is obtained in the complex impedance plots for all samples at high frequencies, which begins at the origin, with the exception of the LZP and LSP samples. The straight line at low frequencies is due to the ion-blocking electrode polarization. This is attributed to the accumulation of the mobile charge carriers at the electrolyte/electrode interface, indicating that the material is an ionic conductor.[38] The separation of grain and grain boundary resistance from the impedance spectra of $Li_{1+x}Sc_xZr_{2-x}(PO_4)_3$ samples is therefore not possible at room temperature. Mariappan et al. and Wolfenstine et al. have investigated the impedance properties of Y-doped and Sr-doped LZP,

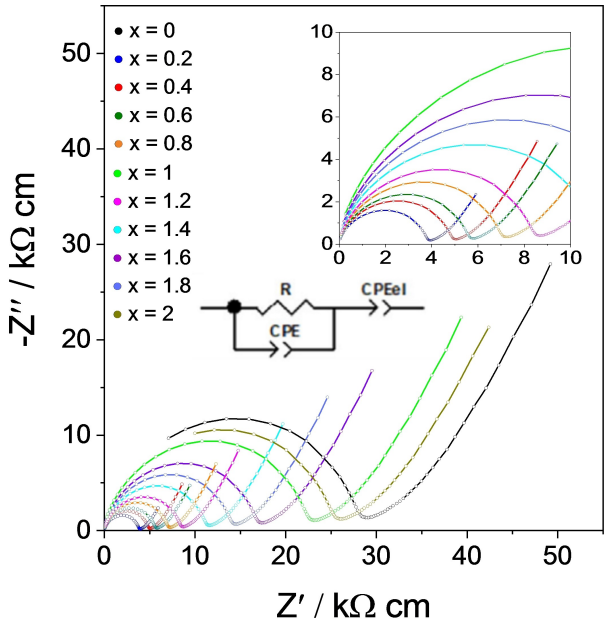

Figure 4. Nyquist plot of impedance spectra at 25 °C of $Li_{1+x}Sc_xZr_{2-x}(PO_4)_3$ where $0 \le x \le 2$ after accounting for the sample dimensions. The equivalent circuit is also shown.

Table 4. Free sintering temperature and time, relative density, and ionic conductivity at 25 °C for $Li_{1+x}Sc_xZr_{2-x}(PO_4)_3$ ($0 \le x \le 2$).

x	Material	Sintering temperature [°C] and dwell time [h]	Relative density [%]	$\sigma_{25\,°C}$ [S cm^{-1}]
0	$LiZr_2(PO_4)_3$	1300/3	88	5.4×10^{-7}
0.2	$Li_{1.2}Sc_{0.2}Zr_{1.8}(PO_4)_3$	1280/3	85	2.7×10^{-5}
0.4	$Li_{1.4}Sc_{0.4}Zr_{1.6}(PO_4)_3$	1250/3	90	9.7×10^{-6}
0.6	$Li_{1.6}Sc_{0.6}Zr_{1.4}(PO_4)_3$	1250/3	98	8.2×10^{-6}
0.8	$Li_{1.8}Sc_{0.8}Zr_{1.2}(PO_4)_3$	1250/3	98	7.1×10^{-6}
1	$Li_2ScZr(PO_4)_3$	1200/3	97	8.2×10^{-7}
1.2	$Li_{2.2}Sc_{1.2}Zr_{0.8}(PO_4)_3$	1230/3	96	6.5×10^{-6}
1.4	$Li_{2.4}Sc_{1.4}Zr_{0.6}(PO_4)_3$	1250/3	94	5.6×10^{-6}
1.6	$Li_{2.6}Sc_{1.6}Zr_{0.4}(PO_4)_3$	985/3	90	2.7×10^{-6}
1.8	$Li_{2.8}Sc_{1.8}Zr_{0.2}(PO_4)_3$	1150/3	91	4.5×10^{-6}
2	$Li_3Sc_2(PO_4)_3$	1000/3	87	6.5×10^{-7}

respectively,[12,39] and reported that the deconvolution of grain and grain boundary resistances for these materials is not feasible. The radius of the semicircle represents the increase of resistivity with increasing *x*. However, this trend is not evident for the unsubstituted sample LZP.

The impedance data were fitted using the given equivalent circuit, as shown in Figure 4. The scandium substitution generates a decrease in the total resistance and improves the ionic conductivity until $x = 0.2$ (see Table 4). With scandium substitution in LZP, the total ionic conductivity at 25 °C increases from 5.4×10^{-7} S cm^{-1} for the unsubstituted LZP to 2.7×10^{-5} S cm^{-1} for $Li_{1.2}Sc_{0.2}Zr_{1.8}(PO_4)_3$, showing the highest ionic conductivity in the $Li_{1+x}Sc_xZr_{2-x}(PO_4)_3$ series and exhibiting a higher ionic conductivity compared to reported values (Figure 5, Table S6, supporting information). $Li_{1.2}Sc_{0.2}Zr_{1.8}(PO_4)_3$ was used to determine the bulk conductivity by impedance spectroscopy measurements below room temperature. In fact, temperature-dependent measurements between −40 °C and 100 °C revealed two overlapping semicircles at low temperatures. From the fitted spectra the bulk ionic conductivity could be determined and the value at 25 °C amounted to 1.46×10^{-4} S cm^{-1}. This value is about one order of magnitude higher than the total conductivity, corresponding well to other Li^+ and Na^+ ionic conductors.[40] The experimental details are summarized in the Supporting Information (Figure S2).

As *x* increases further ($x > 0.2$), ionic conductivity decreases continuously. However, at 25 °C, all scandium-substituted materials show ionic conductivity many times higher than that

Research Article
doi.org/10.1002/batt.202200327
Chemistry Europe
European Chemical Societies Publishing

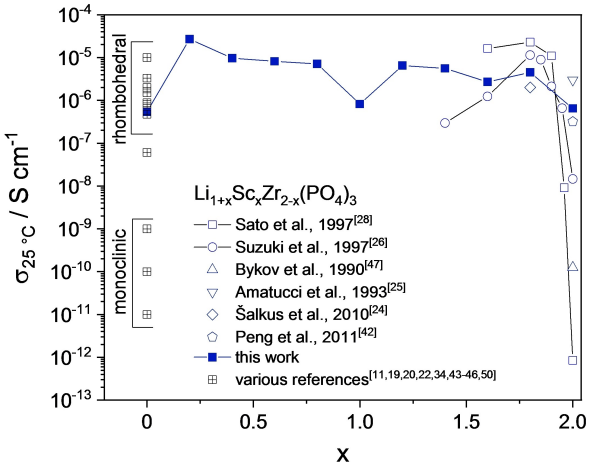

Figure 5. Variation of the total conductivity of $Li_{1+x}Sc_xZr_{2-x}(PO_4)_3$ as a function of *x*. The ionic conductivity of $LiZr_2(PO_4)_3$ (crossed squares) can be divided up into the dimorphic nature of the material. The literature data are listed in the supporting information (Table S6).

of pure LZP.[10,34,41] Even the LSP exhibits a high ionic conductivity of 6.5×10^{-7} S cm^{-1} at RT.

Figure 5 gives an overview of the variation of the total ionic conductivity at 25 °C of $Li_{1+x}Sc_xZr_{2-x}(PO_4)_3$ where $0\le x\le2$. It also contains a literature review of different compositions where $x=0$,[20,22,34,39,42-46] $x=2$,[25,47,48] $x=1.8$,[24] $1.6\le x\le2$,[28] and $1.4\le x\le2$.[26] In this work, at 25 °C, the highest ionic conductivity of this series was observed for the material where $x=0.2$ (2.7×10^{-5} S cm^{-1}). This high value of ionic conductivity could not be associated with densification, since the relative density of this material after one-step sintering was only 85%. However, the density was improved with a two-step sintering approach, as described in Section 3.4. The purity of the material could explain this high value of ionic conductivity, as it is the only material in the series that was indexed as a pure rhombohedral NaSICON phase without any trace of other impurities. In contrast, the $Li_2ScZr(PO_4)_3$ material with a higher relative density (97%) was obtained using the one-step sintering process, but yielded poor ionic conductivity (8.2×10^{-7} S cm^{-1}) at 25 °C. Although XRD analysis (Figure 2) clearly showed the presence of a mixture of rhombohedral and monoclinic phases for $0.4\le x\le1.4$ and rhombohedral, monoclinic, and orthorhombic phases for $1.6\le x\le2$, their conductivities are

higher. Therefore, the low conductivity of $Li_2ScZr(PO_4)_3$ can be considered as a local minimum along the series.

As previously reported, the $Li_{1+x}Sc_xZr_{2-x}(PO_4)_3$ materials where $1.6<x<2$ show similar conductivities: higher than the data of Šalkus et al. ($x=1.8$; 2×10^{-6} S cm^{-1}),[24] but lower than the values reported by Suzuki et al.[26] and Sato et al.[28] On the one hand, the lower reported values of ionic conductivity could be related to a low relative density, which was reported to be only 70%, while 91% was obtained in this work. On the other hand, the higher reported ionic conductivity could be explained by the better homogeneity and the absence of polymorphism in contrast to the $Li_{1+x}Sc_xZr_{2-x}(PO_4)_3$ material investigated here.

For the end members LZP ($x=0$) and LSP ($x=2$), the conductivities at 25 °C vary by about seven orders of magnitude.

This strong scatter is largely dependent on the quality and thermal history of the materials and can be explained by the following reasons: a) Depending on the heat treatment and processing (e.g., quenching), the rhombohedral high-temperature phase can be stabilized below room temperature. This is well known for LZP.[34,44] In turn, crystal symmetry strongly affects the ionic conductivity.[43,44] b) Heat treatment and processing also affect the relative density, and there are many examples where conductivity decreases exponentially with increasing porosity. c) The final stoichiometry of the material is very important, especially for the end members, since small deviations of charge carriers (or vacancies at the other extreme) of only 1–2% can lead to conductivity changes by several orders of magnitude.[49,50]

Yttrium substitutions: $Li_{1+x}Y_xZr_{2-x}(PO_4)_3$ ($0\le x\le2$)

Yttrium was substituted for zirconium in $Li_{1+x}Y_xZr_{2-x}(PO_4)_3$ in a stepwise manner from $x=0$ to $x=2$. According to the shrinkage behavior of the $Li_{1+x}Y_xZr_{2-x}(PO_4)_3$ pellets (see Figures S1b and 14a for the material where $x=0.2$) recorded with dilatometry, the pressed pellets were sintered at different temperatures. The sintering experiments in the furnace were again carried out between $T_{10\%}$ and $T_{23\%}$ in steps of 10 °C in air. The optimal sintering temperatures leading to the highest relative densities are listed in Tables 1 and 7. For materials where $x\ge1$, sintering experiments were performed only from 900 °C to 1000 °C, as dilatometry measurements showed volume expansion starting at around 1010 °C, and sintering experiments in the furnace led to deformation and partial melting.

Figure 6 shows the reflections in the powder XRD patterns of $Li_{1+x}Y_xZr_{2-x}(PO_4)_3$ after sintering at optimum sintering conditions (Tables 1 and 7). The reflections observed for the sample where $x=0.2$ were assigned to a pure and well-crystallized rhombohedral ($R\bar{3}c$) NaSICON structure. $Li_{1+x}Y_xZr_{2-x}(PO_4)_3$ where $x=0.4$ crystallized as a mixed rhombohedral ($R\bar{3}c$) and orthorhombic (*Pbcn*) NaSICON structure. The materials where $0.6\le x\le1.6$ contained the polymorph with the orthorhombic symmetry (*Pbcn*). Furthermore, tetragonal YPO_4 (space group $I4_1/amd$; ICSD no. 201131)[51] was detected as a secondary phase for $0.4\le x\le1.6$, as also observed by Li et al.[21] Starting from $x=0.8$, but especially at $x=1.8$ and $x=2$, YPO_4 appeared as a predominant phase with 95 wt.% and 93 wt.%, respectively. Moreover, small amounts (2–7 wt.%) of orthorhombic Li_3PO_4 (space group *Pcmn*; ICSD no.20208)[52] were detected as an impurity in the YPO_4. Li_3PO_4 is easily formed during the synthesis

of $LiZr_2(PO_4)_3$, as described in Ref. [21]. The content of rhombohedral and orthorhombic NaSICON phases as well as

Research Article
doi.org/10.1002/batt.202200327
Chemistry Europe
European Chemical Societies Publishing

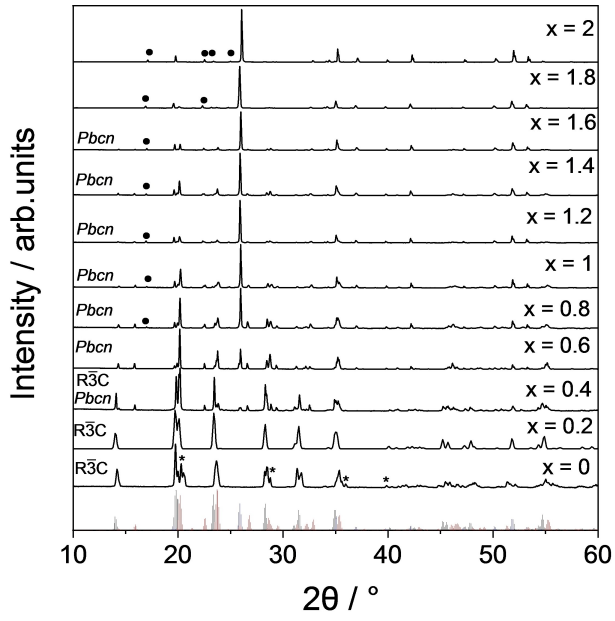

Figure 6. XRD patterns of $Li_{1+x}Y_xZr_{2-x}(PO_4)_3$ where $0 \leq x \leq 2$ after sintering at optimum conditions (Tables 1 and 7). The reference patterns of LYZP are taken from the inorganic crystal structure database (ICSD), R3̄c; ICSD no. 191891(black),[21] Pbcn; ICSD no. 83913 (red),[28] YPO_4 (I41/amd), ICSD no. 201131 (blue).[51] The symbols * and ● indicate $Zr_2O(PO_4)_2$ and Li_3PO_4, respectively.

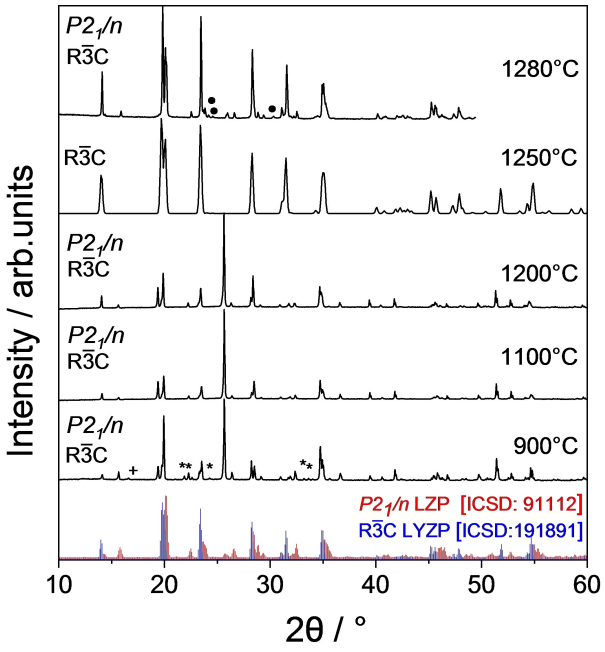

Figure 7. Phase evolution of $Li_{1.2}Y_{0.2}Zr_{1.8}(PO_4)_3$ after sintering at different temperatures from 900 ° C to 1280 °C. The symbols +, *, and ● indicate P_2O_5, YPO_4, and ZrO_2, respectively.

YPO_4 at different Y^{3+} substitution levels from $x = 0.2$ to $x = 1.6$ are summarized in Table 5 and presented in Figure 16(b).

The XRD patterns of $Li_{1.2}Y_{0.2}Zr_{1.8}(PO_4)_3$ from 900 °C to 1200 °C show the presence of a phase mixture of rhombohedral and monoclinic symmetry. At temperatures from 900 °C to 1200 °C, the intensity of reflections associated with the rhombohedral phase increased significantly, and most importantly, at 1250 °C, the material displayed a phase change to pure rhombohedral symmetry. At 1280 °C, in addition to the rhombohedral symmetry, very small reflections of the monoclinic phase were again observed in the pattern (Figure 7).

Unit cell parameters and space group of the $Li_{1.2}Y_{0.2}Zr_{1.8}(PO_4)_3$ after sintering at different temperatures are summarized in Table 6.

Rietveld refinement revealed rhombohedral and monoclinic phase ratios of 40/50 wt.%, 60/40 wt.%, and 80/20 wt.% at 900 °C, 1100 °C, and 1200 °C, respectively. Furthermore, at 900 °C, 2 wt.% of unreacted P_2O_5 with space group *R3̄c* (ICSD no. 16610)[53] and 8 wt.% of tetragonal YPO_4 were detected as secondary phases. At 1280 °C, 20 wt.% of tetragonal ZrO_2 with space group *P4₂/nmc* (ICSD no. 97004)[54] was detected.

The impact of substituting yttrium for zirconium in $Li_{1+x}Y_xZr_{2-x}(PO_4)_3$ on ionic conductivity was also investigated by impedance spectroscopy at 25 °C. The Nyquist plots of the impedance spectra are shown in Figure 8. Here, only the compositions where $0 \leq x \leq 1$ are shown due to the increasing content of YPO_4 in the phase mixture that disproves the conductivity data. Again, at room temperature only one depressed semicircle is obtained at high frequencies starting at zero, except for the compositions $x = 0$ and $x = 1$ whose depressed semicircles did not begin at the origin.

The radius of the semicircle increases with increasing yttrium substitution level from $x = 0.2$ to $x = 1$. Also, here the most conductive material along the series, $Li_{1.2}Y_{0.2}Zr_{1.8}(PO_4)_3$,

Table 5. Lattices parameters, unit cell volume, and space group of LYZP where ($0.2 \leq x \leq 1.6$).

x	Material	a [Å]	b [Å]	c [Å]	V [Å³]	Space group	Content [wt.%]	Content YPO_4 [wt.%]
0.2	$Li_{1.2}Y_{0.2}Zr_{1.8}(PO_4)_3$	8.872(2)	8.872(2)	22.221(1)	1514.74	*R3̄c*	100	0
0.4	$Li_{1.4}Y_{0.4}Zr_{1.6}(PO_4)_3$	8.869(3)	8.869(3)	22.14(1)	1508.20	*R3̄c*	61	6
		8.829(9)	12.438(5)	8.948(9)	982.67	*Pbcn*	33	
0.6	$Li_{1.6}Y_{0.6}Zr_{1.4}(PO_4)_3$	8.831(3)	12.41(1)	8.951(1)	981.99	*Pbcn*	85	15
0.8	$Li_{1.8}Y_{0.8}Zr_{1.2}(PO_4)_3$[*]	8.819(1)	12.41(3)	8.921(2)	976.35	*Pbcn*	26	72
1	$Li_2YZr(PO_4)_3$[*]	8.804(2)	12.372(1)	8.903(2)	969.74	*Pbcn*	30	68
1.2	$Li_{2.2}Y_{1.2}Zr_{0.8}(PO_4)_3$*	8.888(3)	12.355(1)	8.818(3)	968.31	*Pbcn*	35	63
1.4	$Li_{2.4}Y_{1.4}Zr_{0.6}(PO_4)_3$[*]	8.886(2)	12.344(3)	8.820(3)	967.45	*Pbcn*	37	61
1.6	$Li_{2.6}Y_{1.6}Zr_{0.4}(PO_4)_3$[*]	8.882(3)	12.30(3)	8.830(2)	964.66	*Pbcn*	38	59

[*]: Contains 2–7 wt.% Li_3PO_4

Research Article
doi.org/10.1002/batt.202200327
Chemistry Europe
European Chemical Societies Publishing

Table 6. Unit cell parameters and space group of the $Li_{1.2}Y_{0.2}Zr_{1.8}(PO_4)_3$ after sintering at different temperatures.

Temp. [°C]	*a* [Å]	*b* [Å]	*c* [Å]	*β* [°]	*V* [Å³]	Space group
900	8.869(1)	8.869(1)	22.134(2)	90	1507.79	$R\bar{3}c$
	8.876(2)	8.944(1)	12.468(3)	89.903	989.8	*P21n*
1000	8.872(1)	8.872(1)	22.157(2)	90	1510.37	$R\bar{3}c$
	8.857(2)	8.941(1)	12.475(1)	89.902	987.8	*P21n*
1200	8.883(2)	8.883(2)	22.148(1)	90	1513.51	$R\bar{3}c$
	8.861(1)	8.919(1)	12.475(3)	89.801	985.9	$P2_1n$
1250	8.872(2)	8.872(2)	22.221(1)	90	1514.74	$R\bar{3}c$
1280	8.885(3)	8.885(3)	22.181(1)	90	1516.44	$R\bar{3}c$

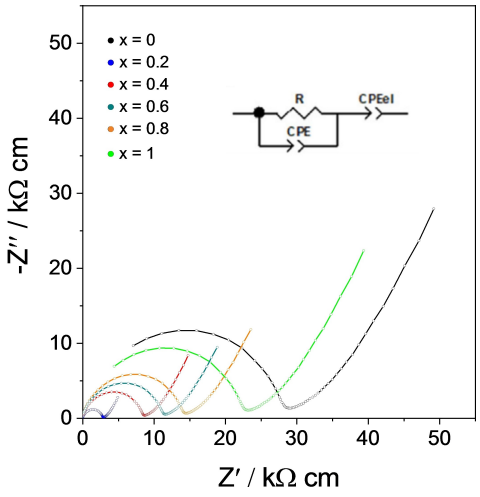

Figure 8. Nyquist plot of impedance spectra at 25 °C of $Li_{1+x}Y_xZr_{2-x}(PO_4)_3$ where $0 \le x \le 1$ after accounting for the sample dimensions. The equivalent circuit is also shown.

was used to determine the bulk conductivity by impedance spectroscopy measurements below room temperature. In this case, however, only one semicircle was observed even at −40 °C. Therefore, a deconvolution of bulk and grain boundary resistance was not possible (see Figure S2).[12,39]

The resistance was obtained by fitting the impedance spectra using the given equivalent circuit in Figure 8. The total conductivity σ_t of the samples was calculated using Equation (2) and the values are listed in Table 7. Initially, the yttrium substitution in $Li_{1+x}Y_xZr_{2-x}(PO_4)_3$ leads to an increase in ionic conductivity. The total ionic conductivity at 25 °C increases from 5.4×10^{-7} S cm^{-1} for LZP to 6.7×10^{-5} S cm^{-1} for $Li_{1.2}Y_{0.2}Zr_{1.8}(PO_4)_3$ as the highest ionic conductivity in the $Li_{1+x}Y_xZr_{2-x}(PO_4)_3$ series and exhibits a higher ionic conductivity in comparison to the reported values for the same stoichiometry,[12,21] as listed in Table S6 and shown in Figure 9. The maximum value of ionic conductivity for $Li_{1.2}Y_{0.2}Zr_{1.8}(PO_4)_3$ is comparable to that of a similar material ($x = 0.15$) sintered by spark plasma sintering (SPS), displaying a conductivity value of 7.1×10^{-5} S cm^{-1}. The influence of the different sintering process is discussed in Section 3.4.

As x increases further ($x > 0.2$), the ionic conductivity decreases continuously with a sharp decline at $x = 1$, which is attributed to the rhombohedral → orthorhombic phase transition and the increasing amount of YPO_4 phase, which was also reported elsewhere.[21] However, at 25 °C, all yttrium-containing materials show an ionic conductivity several times higher than that of LZP.[10,34,41]

Aluminum substitutions: $Li_{1+x}Al_xZr_{2-x}P_3O_{12}$ ($0 \le x \le 1$)

Aluminum was substituted for zirconium in $Li_{1+x}Al_xZr_{2-x}(PO_4)_3$ from $x = 0$ to $x = 1$. According to the shrinkage behavior of the $Li_{1+x}Al_xZr_{2-x}(PO_4)_3$ pellets (see Figures S1c and 14a for the material where $x = 0.2$) recorded with dilatometry, the pressed pellets were sintered at different temperatures between $T_{10\%}$ and $T_{23\%}$ in steps of 10 °C in air. The optimal sintering temperatures leading to the highest relative densities are listed in Tables 1 and 10. For the material where $x = 1$, the sintering experiments were performed only from 900 °C to 950 °C; higher sintering temperatures resulted in melting.

The XRD patterns of $Li_{1+x}Al_xZr_{2-x}(PO_4)_3$ are shown in Figure 10. For $x > 0.2$, all compositions were identified as a phase mixture of rhombohedral and monoclinic symmetry. Impurity peaks can be observed in materials where $x \ge 0.4$ and were attributed to trigonal $AlPO_4$ with space group $P3_12_1$ (ICSD no. 33746).[55] The impurity peaks increase in intensity with increasing Al^{3+} substitution. This could be related to the limited solubility and the low sintering temperatures, since the

Table 7. Free sintering temperature and time, relative density, and ionic conductivity at 25 °C for $Li_{1+x}Y_xZr_{2-x}(PO_4)_3$ ($0 \le x \le 1$).

x	Material	Sintering temperature [°C] and dwell time [h]	Relative density [%]	$\sigma_{25\,°C}$ [S cm^{-1}]
0	$LiZr_2(PO_4)_3$	1300/3	88	5.4×10^{-7}
0.2	$Li_{1.2}Y_{0.2}Zr_{1.8}(PO_4)_3$	1250/3	89	6.7×10^{-5}
0.4	$Li_{1.4}Y_{0.4}Zr_{1.6}(PO_4)_3$	1250/3	94	4.8×10^{-5}
0.6	$Li_{1.6}Y_{0.6}Zr_{1.4}(PO_4)_3$	1250/3	94	3.9×10^{-5}
0.8	$Li_{1.8}Y_{0.8}Zr_{1.2}(PO_4)_3$	1100/3	91	2.7×10^{-5}
1	$Li_2YZr(PO_4)_3$	980/3	89	7.5×10^{-7}

Research Article
doi.org/10.1002/batt.202200327
Chemistry Europe
European Chemical Societies Publishing

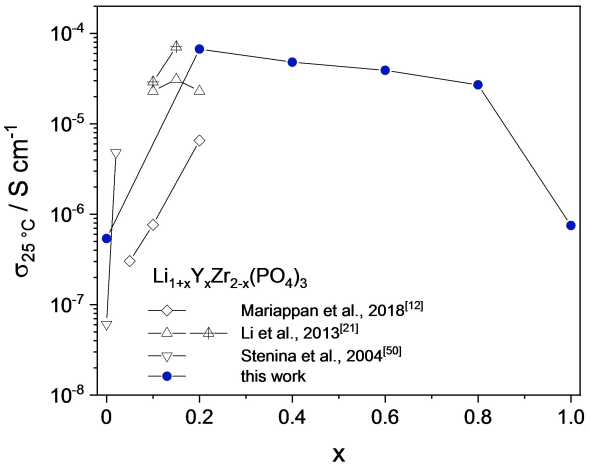

Figure 9. Variation of total conductivity of $Li_{1+x}Y_xZr_{2-x}(PO_4)_3$ as a function of *x*. The crossed triangles denote the samples densified by spark plasma sintering. The literature data are listed in the supporting information (Table S6). For the ionic conductivity data of $LiZr_2(PO_4)_3$, see Figure 6.

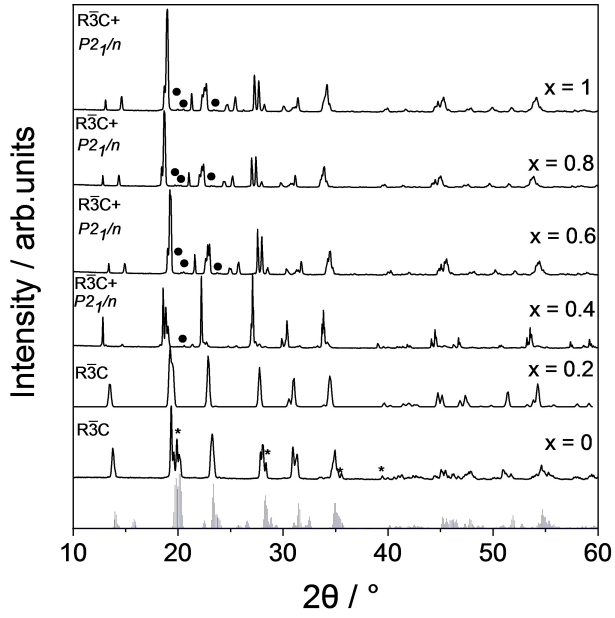

Figure 10. XRD patterns of $Li_{1+x}Al_xZr_{2-x}(PO_4)_3$ where $0 \leq x \leq 1$ after sintering at optimum conditions (Tables 1 and 10). The symbols * and ● indicate $Zr_2O(PO_4)_2$ and $AlPO_4$, respectively. For the reference patterns at the bottom, see Figure 2.

materials where $x = 0.6$, 0.8, and 1 have melting points of 1070 °C, 1032 °C, and 965 °C, respectively.

The unit cell volumes shown in Table 8 decrease with increasing *x* in $Li_{1+x}Al_xZr_{2-x}(PO_4)_3$ ($0 \leq x \leq 1$). Since the ionic radius of Al^{3+} is much smaller than that of Zr^{4+}, this trend is anticipated. While the rhombohedral lattice parameters almost remain constant where $x \geq 0.6$, indicating the solubility limit of Al^{3+} in the lattice, the monoclinic lattice parameters continue to decrease slightly. This result is in good agreement with reported data.[22] For comparison, the rhombohedral lattice parameters and unit cell volume were converted to monoclinic symmetry (space group $P2_1/n$) for all $Li_{1+x}Al_xZr_{2-x}(PO_4)_3$ compositions. The data are summarized in Table S4.

The XRD patterns of $Li_{1.2}Al_{0.2}Zr_{1.8}(PO_4)_3$ from 900 °C to 1250 °C is shown in Figure 11 and clearly show the presence of a mixture of phases with rhombohedral and monoclinic symmetry up to 1200 °C. As the temperature increased, the intensity of the reflections of the rhombohedral phase increased significantly, and at 1250 °C the rhombohedral phase stabilized. The lattice parameters obtained after Rietveld refinement are listed in Table 9. Furthermore, trigonal $AlPO_4$ was detected as a secondary phase from 900 °C to 1200 °C. This secondary phase formation was also reported by Amatucci et al. for $Li_3Sc_{2-x}Al_x(PO_4)_3$.[25]

The resistance was obtained by fitting the impedance spectra (Figure 12) using the given equivalent circuit. The total

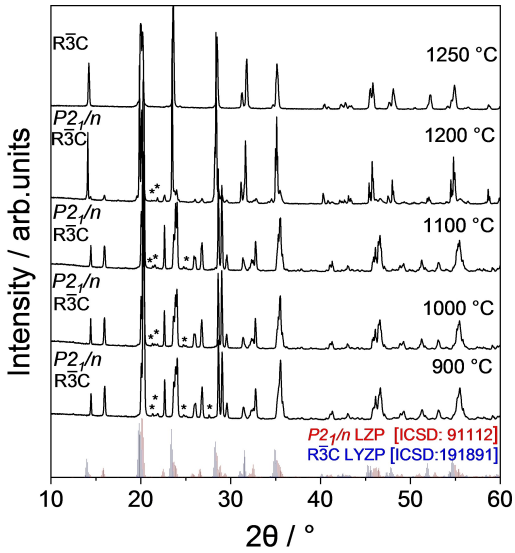

Figure 11. Phase evolution of $Li_{1.2}Al_{0.2}Zr_{1.8}(PO_4)_3$ after different sintering temperatures from 900 ° C to 1250 °C. *: $AlPO_4$.

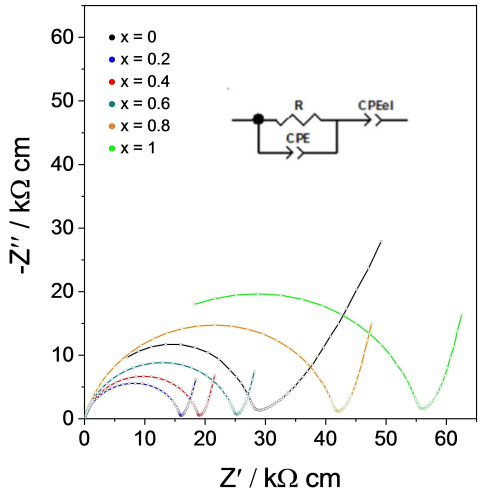

Figure 12. Nyquist plot of impedance spectra at 25 °C for $Li_{1+x}Al_xZr_{2-x}(PO4)_3$ where $0 \leq x \leq 1$ after accounting for the sample dimensions. The equivalent circuit used for the fitting is shown in the inset.

Research Article
doi.org/10.1002/batt.202200327
Chemistry Europe
European Chemical Societies Publishing

Table 8. Lattices parameters, unit cell volume, and space group of $Li_{1+x}Al_xZr_{2-x}(PO_4)_3$ where $0.2 \leq x \leq 1$.

x	Material	a [Å]	b [Å]	c [Å]	β [°]	V [Å^3]	Space group	Content [wt.%]
0.2	$Li_{1.2}Al_{0.2}Zr_{1.8}(PO_4)_3$	8.858(1)	8.858(1)	22.140(1)	90	1504.46	$R\bar{3}c$	98
0.4	$Li_{1.4}Al_{0.4}Zr_{1.6}(PO_4)_3$	8.841(2)	8.841(2)	22.081(3)	90	1494.69	$R\bar{3}c$	82
		8.803(1)	8.929(3)	12.379(1)	89.801	973.01	$P2_1/n$	15
0.6	$Li_{1.6}Al_{0.6}Zr_{1.4}(PO_4)_3$	8.831(1)	8.831(1)	22.072(2)	90	1490.71	$R\bar{3}c$	71
		8.804(2)	8.897(1)	12.419(2)	89.974	972.68	$P2_1/n$	25
0.8	$Li_{1.8}Al_{0.8}Zr_{1.2}(PO_4)_3$	8.831(2)	8.831(2)	22.071(1)	90	1490.64	$R\bar{3}c$	60
		8.810(1)	8.872(2)	12.391(2)	90.015	968.51	$P2_1/n$	35
1	$Li_2AlZr(PO_4)_3$	8.831(2)	8.831(2)	22.070(1)	90	1490.57	$R\bar{3}c$	53
		8.807(1)	8.869(1)	12.388(1)	89.987	967.62	$P2_1/n$	42

Table 9. Unit cell parameters and space group of $Li_{1.2}Al_{0.2}Zr_{1.8}(PO_4)_3$ after sintering at different temperatures.

Temp. [°C]	*a* [Å]	*b* [Å]	*c* [Å]	*β* [°]	*V* [Å^3]	Space group
900	8.947(3)	8.947(3)	22.140(1)	90	1534.84	$R\bar{3}c$
	8.792(1)	8.892(1)	12.324(1)	89.801	963.47	$P2_1/n$
1000	8.974(3)	8.974(3)	22.140(2)	90	1544.12	$R\bar{3}c$
	8.791(1)	8.888(1)	12.328(1)	89.801	963.24	$P2_1/n$
1100	8.887(1)	8.887(1)	22.140(2)	90	1514.32	$R\bar{3}c$
	8.801(1)	8.886(2)	12.338(1)	89.801	964.90	$P2_1/n$
1200	8.855(1)	8.855(1)	22.140(1)	90	1503.44	$R\bar{3}c$
	8.817(2)	8.870(1)	12.475(1)	90.009	975.63	$P2_1/n$
1250	8.858(1)	8.858(1)	22.140(1)	90	1504.46	$R\bar{3}c$

Table 10. Sintering temperature and time, relative density, and ionic conductivity at 25 °C for $Li_{1+x}Al_xZr_{2-x}(PO_4)_3$ ($0 \leq x \leq 1$).

x	Material	Sintering temperature [°C] and dwell time [h]	Relative density [%]	$\sigma_{25\,°C}$ [S cm^{-1}]
0	$LiZr_2(PO_4)_3$	1300/3	88	5.4×10^{-7}
0.2	$Li_{1.2}Al_{0.2}Zr_{1.8}(PO_4)_3$	1250/3	94	3.7×10^{-6}
0.4	$Li_{1.4}Al_{0.4}Zr_{1.6}(PO_4)_3$	1100/3	92	9.5×10^{-7}
0.6	$Li_{1.6}Al_{0.6}Zr_{1.4}(PO_4)_3$	1050/3	91	6.8×10^{-7}
0.8	$Li_{1.8}Al_{0.8}Zr_{1.2}(PO_4)_3$	1010/3	90	5.2×10^{-9}
1	$Li_2AlZr(PO_4)_3$	950/3	87	8.3×10^{-11}

conductivity σ_t of the samples is compiled in Table 10. As in the case of $Li_{1.2}Sc_{0.2}Zr_{1.8}(PO_4)_3$ and $Li_{1.2}Y_{0.2}Zr_{1.8}(PO_4)_3$, the material with $x=0.2$ was used to determine the bulk conductivity by low-temperature impedance spectroscopy. However, as for $Li_{1.2}Y_{0.2}Zr_{1.8}(PO_4)_3$, the impedance of bulk and grain boundaries could not be separated.

Figure 13 provides an overview of the evolution of total ionic conductivity at 25 °C for LAZP where $0 \leq x \leq 1$. In addition, literature data of total ionic conductivity (at 30 °C) of different compositions between $x=0$ and $x=0.5$ are included.[22] Electrical characterization of the series revealed a maximum conductivity of 3.7×10^{-6} S cm^{-1} for the sample where $x=0.2$. Further Al substitution resulted in a steady decrease in ionic conductivity to 8.3×10^{-11} S cm^{-1} for $x=1$. At first sight, the evolution of ionic conductivity is related to the phase purity of the samples: $Li_{1+x}Al_xZr_{2-x}(PO_4)_3$ where $x=0.2$ is the only material in the series crystallizing as a pure rhombohedral NaSICON phase, whereas the materials where $0.4 \leq x \leq 1$ clearly showed the presence of a mixture of rhombohedral and monoclinic phases (Figure 10). Indeed, the substitution of Al for Zr in LZP can stabilize the structure to rhombohedral NaSICON at room temperature and increase the ionic conductivity until

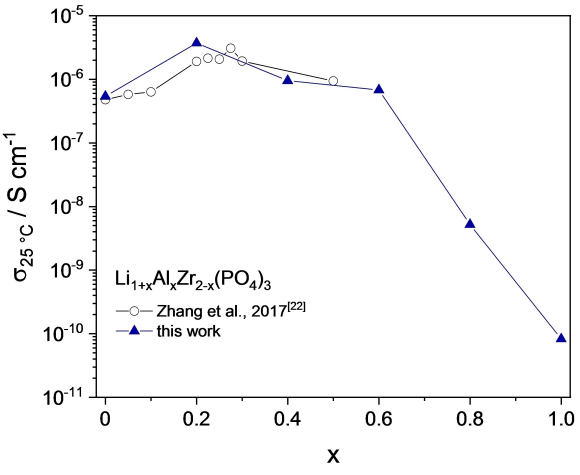

Figure 13. Variation of total conductivity of $Li_{1+x}Al_xZr_{2-x}(PO_4)_3$ as a function of *x*. The literature data are listed in the supporting information (Table S6). For ionic conductivity data of $LiZr_2(PO_4)_3$, see Figure 6.

Research Article
doi.org/10.1002/batt.202200327
Chemistry Europe
European Chemical Societies Publishing

$x = 0.2$. Any further Al substitution resulted in phase mixture and decreasing lattice parameters, which have an adverse influence on ionic conductivity.

The results obtained in this study are slightly higher than the reported values[22] presented in Figure 13. The ionic conductivity of $Li_{1.2}Al_{0.2}Zr_{1.8}(PO_4)_3$ is higher not only in comparison with the same reported material but also with the material where $x = 0.275$, which gave a maximum total ionic conductivity of 3.1×10^{-6} S cm^{-1}.[22]

Optimization of the sintering conditions of $Li_{1.2}M_{0.2}Zr_{1.8}(PO_4)_3$ (M = Sc, Y, Al)

Two-step sintering

The compositions where $x = 0.2$ in the $Li_{1+x}M_xZr_{2-x}P_3O_{12}$ system (M = Al, Sc, Y) showed the highest ionic conductivity for scandium, yttrium, and aluminum substitutions. Therefore, the three compounds with the compositions $Li_{1.2}Sc_{0.2}Zr_{1.8}(PO_4)_3$, $Li_{1.2}Y_{0.2}Zr_{1.8}(PO_4)_3$, and $Li_{1.2}Al_{0.2}Zr_{1.8}(PO_4)_3$ were selected to optimize the sintering conditions, to improve the densification, and to increase the ionic conductivity.

As described above, the shrinkage behavior of the aforementioned compositions was recorded with dilatometry to identify the optimal sintering temperature. The shrinkage was measured during constant heating until a shrinkage of ~23% was reached. The shrinkage curves of the three compounds are shown in Figure 14(a). The pellet of $Li_{1.2}Al_{0.2}Zr_{1.8}(PO_4)_3$ shows several shrinkage steps during the sintering process up to 1100 °C, and no further shrinkage is observed up to 1400 °C. The sample of $Li_{1.2}Sc_{0.2}Zr_{1.8}(PO_4)_3$ shrinks continuously starting from 650 °C, followed by higher shrinkage rates at 1350 °C and 1550 °C, and ending at 18% shrinkage. In the case of $Li_{1.2}Y_{0.2}Zr_{1.8}(PO_4)_3$, a two-stage shrinkage behavior is observed. The pellet shrinks sharply between 800 °C and 1200 °C with up to 18% shrinkage. After a temperature interval without further shrinkage, a second shrinkage starts at about 1400 °C. To reach the optimal sintering conditions for the three compositions, a series of sintering treatments was carried out from 1000 °C to 1300 °C with 10 °C intervals for 3 hours in air (not shown here), for which shrinkage was 7–12% and 11–18%, respectively. Whereas sintering at low temperature resulted in high porosity and low conductivity, sintering at high temperature led to the formation of cracks and lithium evaporation. Furthermore, optimizing the sintering conditions with two-step sintering slightly enhanced the relative density of the sintered pellets of the three materials (Table 11). Such sintering processes have already been used in the past for solid state electrolyte.[56–58]

The resulting densities of the different heat treatments are shown in Figure 14(b). Pellets of $Li_{1.2}Sc_{0.2}Zr_{1.8}(PO_4)_3$ were first exposed to 1280 °C for a short time (0.25 h), followed by annealing at a reduced temperature (980 °C) for a prolonged period of time (3 h). The relative density increased from 82% at 1280 °C/3 h (one-step sintering) to 94% for the two-step sintering protocol (1280 °C/0.25 h and then at 980 °C/3 h). In the case of $Li_{1.2}Y_{0.2}Zr_{1.8}(PO_4)_3$, the two-step sintering method

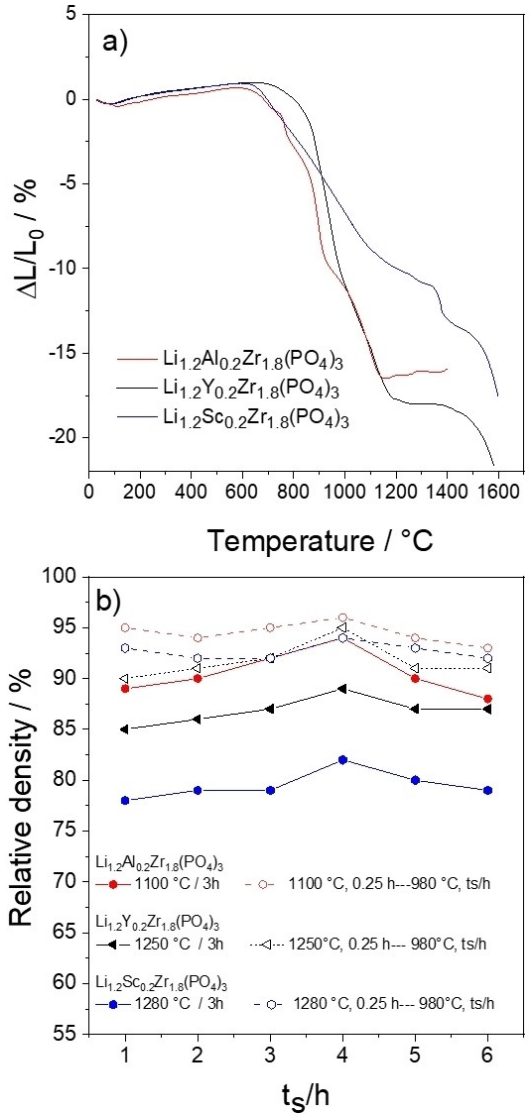

Figure 14. a) Free sintering curves of $Li_{1.2}Sc_{0.2}Zr_{1.8}(PO_4)_3$, $Li_{1.2}Y_{0.2}Zr_{1.8}(PO_4)_3$, and $Li_{1.2}Al_{0.2}Zr_{1.8}(PO_4)_3$ samples up to 1600 °C. b) Relative densities obtained after sintering under different sintering conditions. Filled symbols: one-step sintering; open symbols: two-step sintering.

also resulted in a significant increase of relative density from 89% at 1250 °C/3 h (one-step sintering) to 95% after 1250 °C/0.25 h and then at 980 °C/4 h (two-step sintering). The improvement of the relative density of $Li_{1.2}Al_{0.2}Zr_{1.8}(PO_4)_3$ was not as successful compared to the other two materials. Here, the relative density increased from 94% at 1100 °C/3 h (one-step sintering) to 96% at 1100 °C/0.25 h and then at 980 °C/3 h (two-step sintering).

The two-step sintering method resulted in reproducible relative densities of >90% for all three compositions. This sintering procedure not only increased the density of the specimens, but also reduced the loss of lithium oxide as the samples remained at a high temperature for only a short period of time.

Research Article
doi.org/10.1002/batt.202200327
Chemistry Europe
European Chemical Societies Publishing

Table 11. Comparison of relative densities and ionic conductivity for the $Li_{1.2}M_{0.2}Zr_{1.8}(PO_4)_3$ materials (M = Al, Sc, Y) using different sintering processes.

Material	Sintering process	Sintering temperature [°C] and dwell time [h]	Relative density [%]	$\sigma_{25\,°C}$ [S cm^{-1}]
$Li_{1.2}Sc_{0.2}Zr_{1.8}(PO_4)_3$	One- step-sintering	1280/3	85	2.7×10^{-5}
	Two-step sintering	1280/0.25 + 980/3	94	4.8×10^{-5}
	FAST/SPS	1200/0.17	92	3.4×10^{-5}
$Li_{1.2}Y_{0.2}Zr_{1.8}(PO_4)_3$	One- step-sintering	1250/3	89	6.7×10^{-5}
	Two-step sintering	1250/0.25 + 980/3	95	7.3×10^{-5}
	FAST/SPS	1150/0.17	94	7.0×10^{-5}
$Li_{1.2}Al_{0.2}Zr_{1.8}(PO_4)_3$	One- step-sintering	1250/3	94	3.7×10^{-6}
	Two-step sintering	1250/0.25 + 980/3	96	7.1×10^{-6}
	FAST/SPS	1050/0.17	95	4.5×10^{-6}

FAST/SPS

The two-step sintering process was very helpful in optimizing the sintering conditions and improving the densification process, but the dwell time is a parameter that needs to be improved further. Therefore, to reduce the dwell time as well as the sintering temperatures, the three selected materials were sintered by high-pressure FAST/SPS for 0.17 hours at temperatures of 1200 °C, 1150 °C, and 1050 °C for $Li_{1.2}Sc_{0.2}Zr_{1.8}(PO_4)_3$, $Li_{1.2}Y_{0.2}Zr_{1.8}(PO_4)_3$, and $Li_{1.2}Al_{0.2}Zr_{1.8}(PO_4)_3$, respectively. As a result, higher relative densities were obtained compared to the one-step sintering procedure but not as high as in the two-step sintering process. The relative densities of materials sintered by one-step sintering, two-step sintering, and FAST/SPS are listed in Table 11. The two-step sintering method presents a simple alternative compared with FAST/SPS technology, which is a complex fabrication route and therefore industrially less viable.[59] Table 11 also shows that the ionic conductivity was improved for the three compositions due to the increased relative density.

Figure 15 shows SEM images of fracture surfaces of sintered pellets of $Li_{1.2}M_{0.2}Zr_{1.8}(PO_4)_3$ where M = Al, Sc, Y after sintering by one-step sintering, two-step sintering, and FAST/SPS. In terms of the homogeneity of the materials, the SEM images show that the two-step sintering process gives the best results of the three samples compared to the other two sintering processes. The two-step sintering process resulted in low porosity and an almost crack-free microstructure without areas

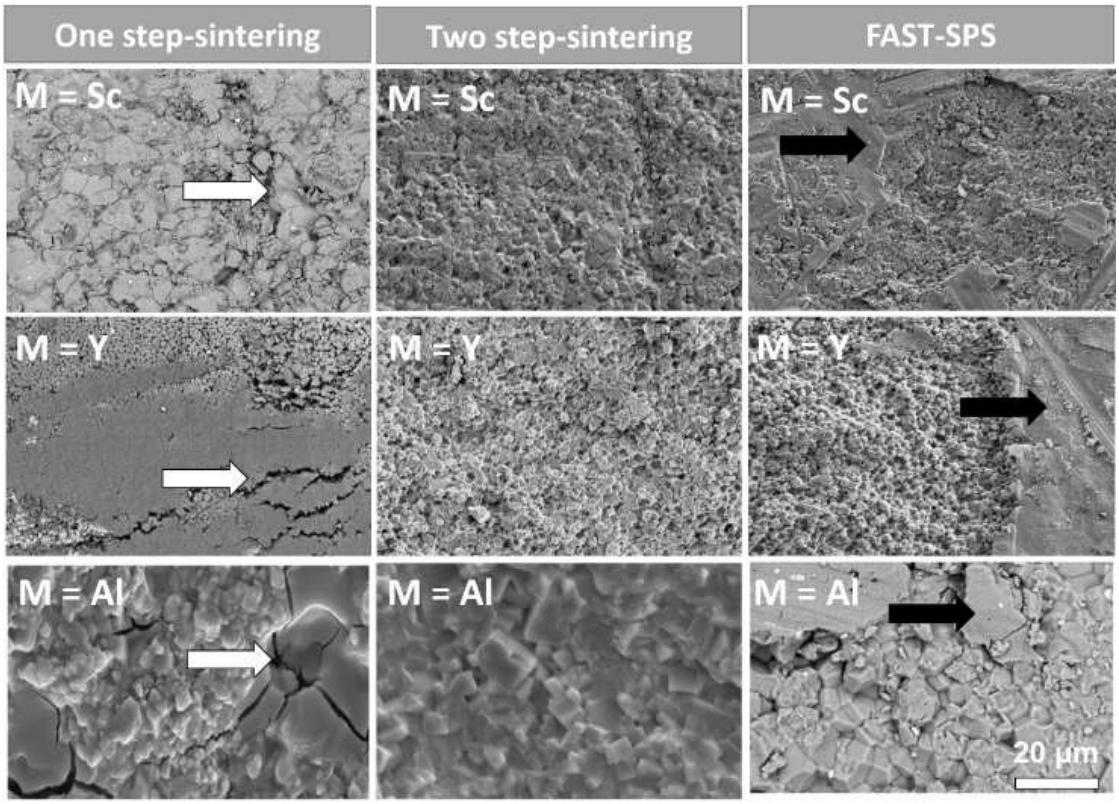

Figure 15. SEM images showing the microstructure of $Li_{1.2}M_{0.2}Zr_{1.8}(PO_4)_3$ (M = Al, Sc, Y) after sintering at different temperatures and dwell times (Table 10). The white arrows indicate the micro-cracks and the black arrows show the areas with partial melting.

of partial melting. In comparison, the one-step sintering process leads to crack formation in all samples due to stronger grain growth, while FAST/SPS enhances the partial melting of materials where M = Sc, Y, although this is not pronounced in the case of M = Al. The SEM analyses provided the following observations:

a) Sintering at high temperatures for a long time in the furnace using the one-step sintering resulted in the formation of pores and micro-cracks, which can be related to the evaporation of Li_2O and accelerated grain growth, respectively. Weight loss related to the evaporation of Li_2O was observed by DTA/TG measurements (not shown here) in the range of 1250 °C to 1300 °C.
b) The formation of micro-cracks is minimized by the two-step sintering because the sample remains at a high temperature for only a short period of time.
c) Partial melting after the FAST/SPS process, as observed predominantly in materials where M = Sc, Y, can be associated with the high temperatures applied, while this phenomenon is far less visible for M = Al because of the lower sintering temperature (Table 11). Therefore, a lower sintering temperature leads to compact materials and high densification, as shown in the SEM images for M = Al by two-step sintering and FAST/SPS.

Discussion of the substitution-dependent chemistry

The evolution of the refined content of the rhombohedral, monoclinic, and orthorhombic NaSICON phases and the unit cell volumes as a function of x in $Li_{1+x}M_xZr_{2-x}P_3O_{12}$ (M = Al, Sc, Y) is depicted in Figure 16. For better comparison of the unit cell volumes among the different space groups, the crystallographic data of rhombohedral and orthorhombic phases were converted to the monoclinic cell volume.

The substitution of Zr^{4+} with Sc^{3+} in $Li_{1+x}Sc_xZr_{2-x}(PO_4)_3$ ($0 \leq x \leq 2$) stabilized the pure rhombohedral phase at RT for the composition $x = 0.2$. Compositions where $0.4 \leq x \leq 1.4$ have a mixture of phases with rhombohedral and monoclinic symmetry. The rhombohedral phase content decreases while the monoclinic modification increases with the substitution of Sc^{3+} until both phases have an equal content at $x = 1$. In addition to these two phases, the orthorhombic phase appears in compositions where $1.6 \leq x \leq 2$ and increases with the Sc^{3+} substitution. The contents (in wt.%) of the different phases for this series of compositions are listed in Table 2 and presented in Figure 16(a). The evolution of rhombohedral ($0 \leq x \leq 2$), orthorhombic ($1.6 \leq x \leq 2$), and monoclinic unit cell volumes ($0.4 \leq x \leq 2$) generally decreases with increasing x in $Li_{1+x}Sc_xZr_{2-x}(PO_4)_3$. Since Sc^{3+} (0.745 Å) and Zr^{4+} (0.72 Å) have similar ionic radii,[60] the differences in the unit cell volume of the $Li_{1+x}Sc_xZr_{2-x}(PO_4)_3$ series (Figure 16b) are mainly caused by the difference in the Li^+ concentration in the formula unit. For the compositions $x = 1.6$, 1.8, and 2, the difference between the monoclinic and orthorhombic phases is only a slight twist of the unit cell. Since the monoclinic and orthorhombic phases are crystallographically very similar and have almost the same unit cell volume as the rhombohedral phase at $x = 1.8$ and 2, the resulting compounds can be considered to be a single phase with different short- and long-range distortions leading to multiple diffraction peaks in the XRD patterns. These results are consistent with previous work.[28] More crystallographic data can be found in the supporting information (Table S2).

The substitution of Zr^{4+} with Y^{3+} in $Li_{1+x}Y_xZr_{2-x}(PO_4)_3$ causes a decrease of the orthorhombic and rhombohedral unit cell volumes (except for $x = 0.6$, Figure 16d). This trend cannot be caused by the different radii of Y^{3+} and Zr^{4+} ions, as the ionic radius of Y^{3+} (0.9 Å) is significantly larger than that of Zr^{4+} (0.72 Å).[60] Rhombohedral lattice parameters in Ref. [21] are in accordance with the measured values. The previously mentioned substitution stabilized the pure rhombohedral phase at RT for the composition $x = 0.2$, showing the highest ionic conductivity value in this series. The further substitution of Y^{3+} first leads to a mixture of rhombohedral and orthorhombic phases ($x = 0.4$) and then to a pronounced formation of YPO_4 ($0.6 \leq x \leq 2$), resulting in lower ionic conductivity. From Figure 16(c), it can be deduced that the solubility limit of Y^{3+} is about $x = 0.3$. The decrease in ionic conductivity depends firstly on the crystallographic results, i.e., the constricted orthorhombic unit cell volume of the materials where $0.4 \leq x \leq 1.6$, and secondly on the increasing impurity of the materials. The occurrence of both phenomena indicates the extraction of Y and P from the NaSICON phase, leading to different NaSICON compositions than expected. As an example, assuming the complete separation of Y from the NaSICON phase, the $Li_2YZr(PO_4)_3$ compound splits into YPO_4 and $Li_2Zr(PO_4)_2$. Rewriting the latter composition as $Li_3Zr_{1.5}(PO_4)_3$, it can be assumed that NaSICON compositions such as $Li_{2.5}[Zr_{1.5}Li_{0.5}](PO_4)_3$ are formed in which Li^+ ions occupy Zr^{4+} sites, indicated in Figure 1 as the region behind the orange area in the x-y plane. This aberrant NaSICON formation also explains the decreasing unit cell volumes.

Substituting Zr^{4+} with Al^{3+} in $Li_{1+x}Al_xZr_{2-x}P_3O_{12}$ ($0 \leq x \leq 1$) also stabilizes the rhombohedral NaSICON structure at RT for the composition where $x = 0.2$ and decreases the unit cell volume with increasing Al^{3+} content (Figure 16f), since the ionic radius of Al^{3+} (0.535 Å in sixfold coordination) is much smaller than that of Zr^{4+} as anticipated.[60] However, the progressive substitution with Al^{3+} ($x \geq 0.4$) reduces the rhombohedral unit cell volume, resulting in a NaSICON phase mixture with rhombohedral and monoclinic symmetry and leading to the formation of $AlPO_4$. Substituting Zr^{4+} with Al^{3+} reduces the rhombohedral content and increases the monoclinic one (Figure 16e).

Nuclear magnetic resonance investigations confirmed the presence of preferentially octahedral coordinated aluminum (Al_O) in $Li_{1+x}Al_xTi_{2-x}(PO_4)_3$, but with increasing x a significant proportion of Al was also found on tetrahedral sites (Al_T).[61,62] The presence of Al_T can be attributed to the segregation of the $AlPO_4$ phase, which is in good agreement with the XRD results of this work (Figure 10), but also to the limited substitution of P^{5+} (0.17 Å) with Al^{3+} (0.39 Å in fourfold coordination)[59] in the NaSICON structure, presumably leading to the progressive

Research Article
doi.org/10.1002/batt.202200327
Chemistry Europe
European Chemical Societies Publishing

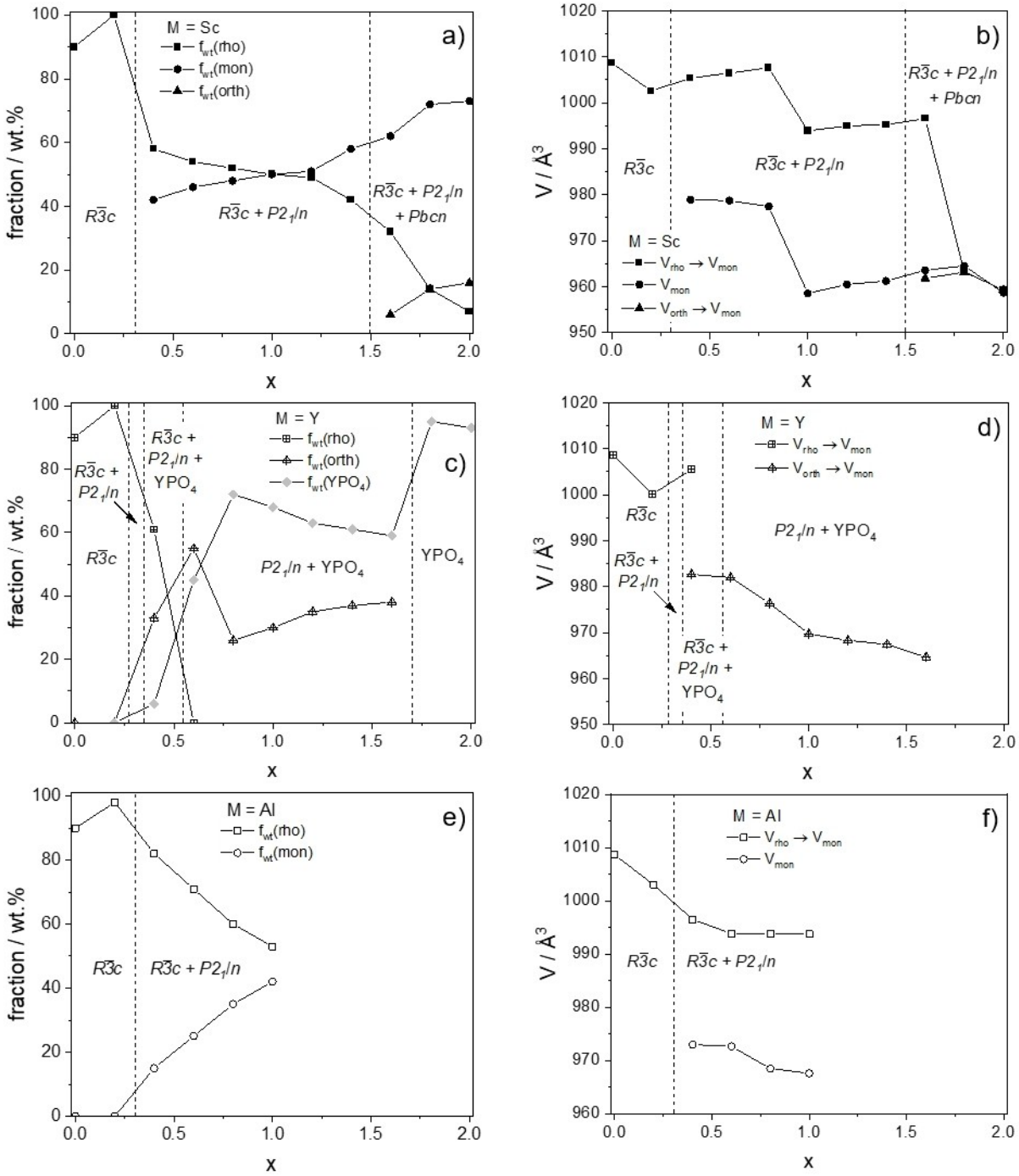

Figure 16. a, c, e) Evolution of the weight fraction of the NaSICON polymorphs (and YPO_4 in c); b, d, f) monoclinic unit cell volume as a function of *x* in $Li_{1+x}M_xZr_{2-x}P_3O_{12}$ where M = Sc, Y, and Al, respectively. Converted lattice parameters and literature data are listed in the Supporting Information.

destabilization of the lattice and the strong decline of ionic conductivity for compounds where $x > 0.6$ (Figure 13).

Electrochemical stability window

Characterization of electrochemical stability window using cyclic voltammetry

In general, oxide and phosphate electrolytes feature higher electrochemical stability and a broader electrochemical window than sulfide, polymer, or liquid electrolytes.[63,64] One of the most promising Li-ion solid electrolytes with a NaSICON

Research Article
doi.org/10.1002/batt.202200327
Chemistry Europe
European Chemical Societies Publishing

structure like LATP, however, still faces challenges in the low voltage range due to the reduction of Ti^{4+} to Ti^{3+} in direct contact with lithium anodes.[65] For this purpose, selected NaSICON electrolytes such as $LiZr_2(PO_4)_3$ (LZP), $Li_{1.2}Y_{0.2}Zr_{1.8}(PO_4)_3$ (LYZP), and $Li_3Sc_2(PO_4)_3$ (LSP) were investigated with regard to their reduction stability range.

Asymmetric cells in which the sintered pellets of the selected materials LZP, LYZP, and LSP were sandwiched between the Au and Li electrodes (Au | NaSICON | Li) were investigated by cyclic voltammetry (CV). Similar characterization was also performed for $Li_{1.5}Al_{0.5}Ti_{1.5}(PO_4)_3$ (LATP) to compare its electrochemical stability window with that of LZP, LYZP, and LSP.

As mentioned earlier, titanium-containing materials are instable against lithium[66] and indeed the cyclic voltammograms of LATP shown in Figure 17(a) confirm the reactions occurring during cycling. A pair of broad quasi-reversible peaks corresponding to the Ti^{4+}/Ti^{3+} redox process is observed at an average potential of about 2.6 V vs. Li^+/Li, with the onset of Ti^{4+} to Ti^{3+} reduction starting as early as ~2.5 V vs. Li^+/Li and the peak potential at ~1.7 V vs. Li^+/Li. The peak of the corresponding oxidation process is observed at ~4.7 V vs. Li^+/Li.[67,68] The current density decreases in the following cycles, indicating a low Coulomb efficiency of this process. These peaks are superimposed on the reduction current at negative potentials below ~1 V, which correspond to the Li plating process with a possible formation of Li alloys (e.g., Li–Au alloy due to the reaction with the Au adhesion layer).[69]

The substitution of Ti^{4+} with Zr^{4+} and Sc^{3+} significantly increases the reduction stability of the resulting compounds, as shown in Figure 17b-d. In contrast to LATP, a reduction process is observed at much more negative potentials in LYZP, with a reduction onset at ~1.5 V vs. Li^+/Li and a peak potential at ~0.5 V vs. Li^+/Li. The cause of this process is still unknown, although it is thought to be the reduction of Zr^{4+},[15] which is in good agreement with the detection of the Zr^{3+} species in the XPS. However, the exact origin of this process and the compounds formed still needs to be confirmed. It should be mentioned, however, that the reduction current is much lower compared to LATP and that the current corresponding to this process decreases sharply in the subsequent cycles. In the reverse scan, a very small peak of an oxidation process is

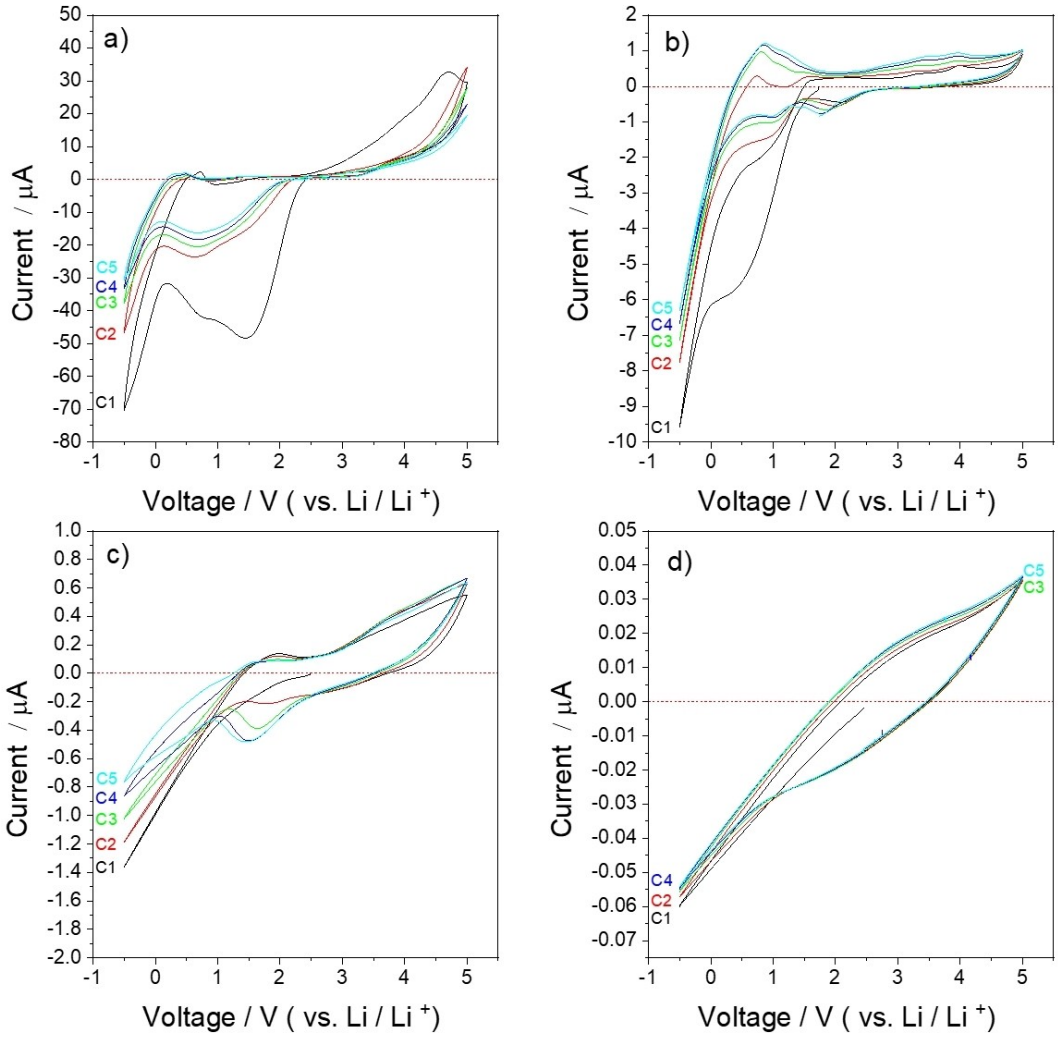

Figure 17. Cyclic voltammograms of a) LATP, b) LYZP, c) LZP, and d) LSP in Au | NaSICON | Li cells ranging from −0.5 to 5 V with a speed of 1 mV s^{-1}.

Research Article
doi.org/10.1002/batt.202200327
Chemistry Europe
European Chemical Societies Publishing

observed at a potential of ~4 V vs. Li^+/Li, and in the second reduction scan, a very small reduction peak is detected at ~1.7 V vs. Li^+/Li. This peak most likely corresponds to the reduction of a compound formed during the oxidation scan, but the origin of this process still needs to be explained.

LZP (Figure 17c) and LSP (Figure 17d) generally exhibit very low currents and poor electrochemical performance due to their low ionic conductivity in the range of 10^{-7} S/cm, and LSP in particular shows near-Ohmic behavior. LZP, similar to LYZP, shows a linear onset of reduction currents at potentials below ~1 V vs. Li^+/Li. These currents can also be attributed to the reduction of Zr^{4+} and Li plating at more negative potentials, which are, however, poorly resolved due to the low ionic conductivity of this compound and the resulting high resistive polarizations. In the oxidation scan, a small oxidation peak is observed at a potential of ~4 V vs. Li^+/Li, with the corresponding reverse reduction peak detected in the second reduction scan. The potential of these peaks is similar to those of LYZP and likely to have the same origin.

LSP (Figure 17d) exhibited the widest electrochemical window of all the compounds studied, with no reduction or oxidation peaks detected in the potential range from −0.5 V to 5 V vs. Li^+/Li, but showed high Ohmic polarization due to its low ionic conductivity.

The conclusions about the reduction stability of the investigated NaSICON materials obtained by CV measurements are in good agreement with the optical appearance of the pellets after contact with Li metal. As shown in Figure 18 b), f), and j), no instant color change was observed for LSP, LZP, and LYZP after direct contact with lithium metal. However, in the case of the LATP electrolyte (Figure 18n), an immediate color change from white to black was clearly observed after direct contact with lithium metal. A longer exposure time with lithium metal of up to 24 h did not lead to a color change in the case of LSP (Figure 18c), while the zirconium-containing materials LZP and LYZP started to react locally, as shown in Figure 18(g and k). In the case of LZP, only isolated black spots were observed, while in the case of LYZP, the majority of the surface was colored black. However, the chemical stability of these materials to Li metal is much higher than that of LATP, which reacted completely with the adhering Li metal and formed a thick black layer on the entire surface.

After a cycling test of asymmetric Au | NaSICON | Li cells at RT for 100 hours, no change was observed on the surface of the LSP pellet, while LZP and LYZP showed some color changes. LZP formed a considerable number of black spots, and the LYZP showed a black layer on the surface of the pellet. However, LATP reacted completely with lithium metal and formed a very thick black layer on the surface, indicating the low stability of the solid electrolyte in contact with lithium.

In order to measure the evolution of the interface resistance (R_i) of a Li/NaSICON/Li cell with impedance spectroscopy, $Li_{1.2}Sc_{0.2}Zr_{1.8}P_3O_{12}$ (LSZP) was coated with Li metal and the measurements were performed first at instantaneous contact with Li metal and then after every 24 hours until 120 hours of contact with Li metal was reached. Fitting the semicircle at low frequencies (Figure S3a) gave increasing R_i values from 3.4 to 4.7 $k\Omega\,cm^2$ with inceasing contact time (Figure S3b). The interfacial resistance between LSZP and Li metal is rather high and after removal of the Li electrodes the surface of the pellet looked very similar to that of LZP (cf. Figure 18h and Figure S4 in the Supporting Information).

The experiments show that LSP has very good chemical stability and no interaction with lithium, indicating the possibility of its direct combination with the lithium metal anode. LYZP and LZP exhibit much higher reduction stability than LATP, but react to some extent in direct contact with lithium metal.

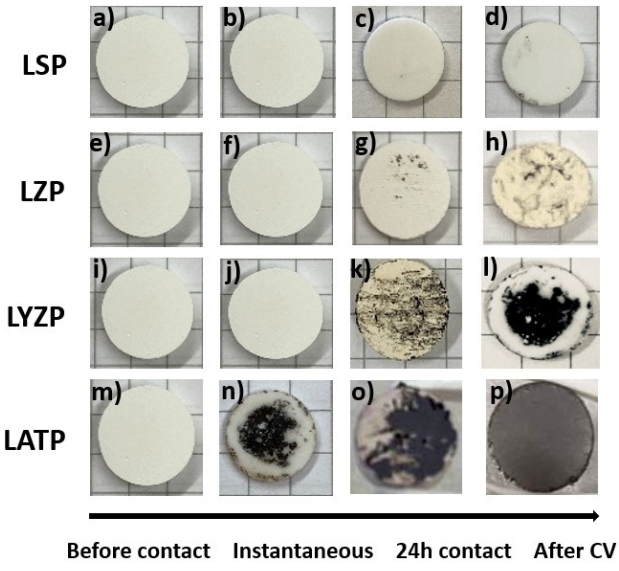

Figure 18. a-d) Pellets of LSP, e-h) LZP, i-l) LYZP and m-p) LATP after different exposure times with metallic lithium. The CV test was performed with Au | NaSICON | Li cells.

Characterization of the black surface layer on $Li_{1.2}Y_{0.2}Zr_{1.8}(PO_4)_3$ after cycling

After the cycling experiments, no indication of phase decomposition was observed by XRD, i.e., the black layer coating the surface of LYZP is most likely very thin or amorphous.

Therefore, XPS measurements were performed to explore the reaction products in more detail. In the first set of experiments, the black surface layer formed after cycling the Au | LYZP | Li cell was investigated. For comparison, a second set of measurements was applied to characterize LYZP after heat treatment at 1000 °C in an inert atmosphere (Ar) for 3 hours. Normalized C 1s, O 1s, P 2p, and Zr 3d XPS spectra of these samples are shown in Figure 19 together with the spectra of the reference sample. As seen in the C 1s spectra, there are slight differences between the samples. The treated samples indicate the formation of a small amount of high binding energy species (e.g., at 288.6 eV). Such a binding energy corresponds to C=O/O–C–O related species, which might also have formed during transport and the exposure of samples to the ambient atmosphere. In the O 1s spectra, the reference

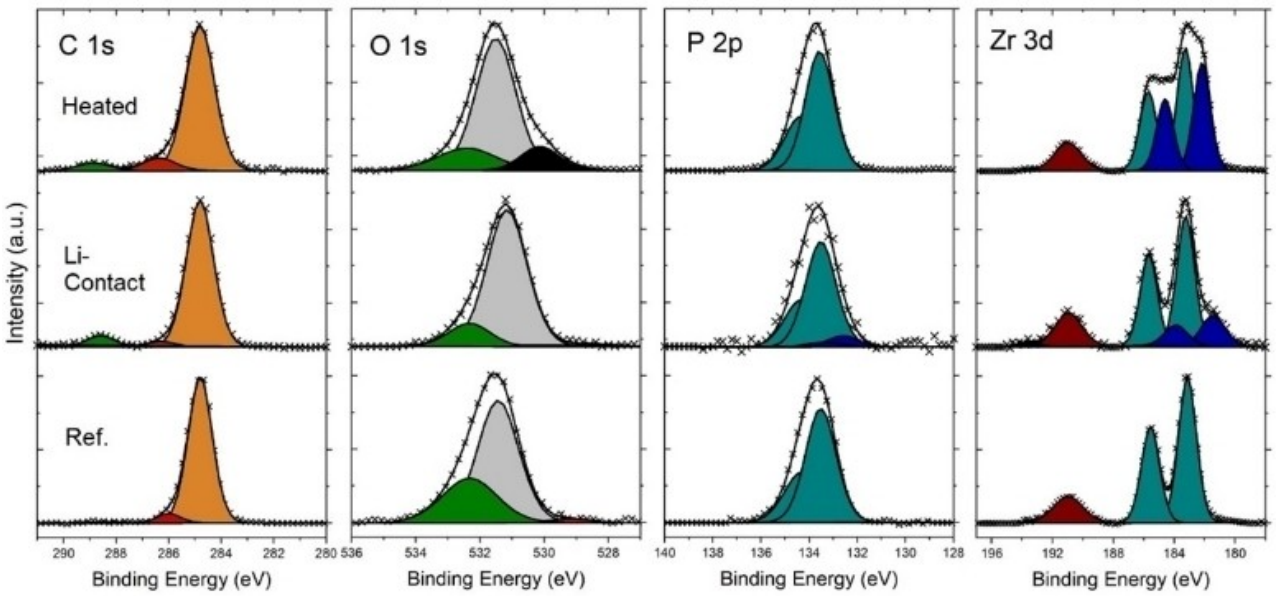

Figure 19. XPS spectra of $Li_{1.2}Y_{0.2}Zr_{1.8}(PO_4)_3$ samples before and after reduction either via Li contact or heating in an Ar atmosphere at 1000 °C. Normalized C 1s, O 1s, P 2p, and Zr 3d spectra from left to right.

sample has two main peaks located at 531.4 eV and 532.3 eV. After contact with Li metal, the position of the low energy peak shifts to around 531.2 eV. However, upon high-temperature heat treatment, a new peak appears at around 530.1 eV. This may originate from near-surface phase transitions or reactions due to the thermal instability of the material in an Ar atmosphere, for example the formation of new oxide phases. Unfortunately, it is not possible to make precise deductions at this binding energy, since many metal oxide compounds exhibit peaks at this energy region.

In the P 2p spectra, all samples seem to consist of closely located spin orbit components of $Li_{1.2}Y_{0.2}Zr_{1.8}(PO_4)_3$. However, the sample that was in contact with Li metal shows a contribution from a new set of peaks, which may originate from the formation of Li_3P at around 133 eV. It has previously been reported that the reaction with Li can result in the formation of Li_8ZrO_6 and Li_3P.[17,70] In this case, however, no additional crystalline phase was observed by XRD, which implies that an amorphous layer may contribute to the shift of the main O 1s peak to a lower binding energy In the heated sample, the shift to a low binding energy is more significant and the contribution can be easily identified with the formation of the third peak (black). This clearly shows that the decomposition products are different for the samples in contact with Li and the heat-treated samples. The Zr 3d spectra also confirm these differences (note that the brown peak in the Zr 3d spectra is due to the P 2 s contribution). For the heat-treated sample, the formation of a lower energy set of spin orbit peaks (shown in blue) is much more intense and positioned at slightly lower energies. The largest 3d 5/2 signal of the reference sample appears at 183.2 eV, which is in very good agreement with the binding energy of 183.1 eV for Zr^{4+} ions in ZrO_2.[71] For the sample that was heat-treated in Ar, the additional doublet appears at a shift of about 1 eV peaking at 182.2 eV of the larger signal. In the case of Li contact, peaks are again shifted to lower energies (largest peak at 181.4 eV). The overall peak shift agrees with a previous study on the interfacial stability of Li and LZP[70] and with the binding energy of Zr^{3+} (182.1–181.8 eV depending on the experimental conditions).[71] Therefore, both reducing conditions lead to the formation of Zr^{3+} ions and are the reason for the black coloration.

Although the relative concentration of decomposition products is not high, depth profiling (Figure S5) shows that the formation of Li-rich compounds is not limited to the surface and can be detected with high intensity after the sputtering process. It shows that the reduced surface of the sample reacted with the atmosphere during storage and transport after the removal of the Li metal contact.

Conclusion

Materials in the $Li_{1+x}M^{3+}{}_xZr_{2-x}(PO_4)_3$ system where M = Al, Sc, Y were synthesized by the solution-assisted solid-state reaction. XRD investigations indicated that the samples contained different polymorphs of the NaSICON structure and crystallized with rhombohedral ($R\bar{3}c$) or monoclinic ($P2_1/n$) symmetries, or a mixture of both. In some cases, reflections of the orthorhombic phase (*Pbcn*) were also detected in addition to those of the $R\bar{3}c$ and $P2_1/n$ symmetries. The purity and crystallographic structure of the materials strongly affected the ionic conductivity. The compositions where $x = 0.2$ in the three systems showed the highest ionic conductivity, as these compositions exhibited high purity and a well-crystallized rhombohedral NaSICON structure. Ionic conductivity significantly increased from 5.4×10^{-7} S cm^{-1} for the unsubstituted $LiZr_2(PO_4)_3$ to 3.6×10^{-6} S cm^{-1}, 2.7×10^{-5} S cm^{-1}, and 6.7×10^{-5} S cm^{-1} for the compositions $Li_{1.2}Al_{0.2}Zr_{1.8}(PO_4)_3$, $Li_{1.2}Sc_{0.2}Zr_{1.8}(PO_4)_3$, and

Research Article
doi.org/10.1002/batt.202200327
Chemistry Europe
European Chemical Societies Publishing

$Li_{1.2}Y_{0.2}Zr_{1.8}(PO_4)_3$, respectively, with a consistent relative density of 94–96%. Therefore, those three compositions were selected from the systems to further optimize sintering conditions, improve densification, and increase ionic conductivity using the two-step sintering method and FAST/SPS. Sintering the materials using the two-step sintering process resulted in the reduction of pores and the minimization of micro-cracks forming. The application of this sintering procedure not only increased the density of the samples, but also reduced the loss of lithium oxide because the samples only remained at a high temperature for a short period of time. Ionic conductivity was improved for the three compositions by increasing the density, and the highest value after optimizing the sintering conditions was increased to $7.3\times10^{-5}\,S\,cm^{-1}$ for the composition $Li_{1.2}Y_{0.2}Zr_{1.8}(PO_4)_3$.

The NaSICON materials $LiZr_2(PO_4)_3$, $Li_{1.2}M_{0.2}Zr_{1.8}(PO_4)_3$ (M = Sc, Y) and $Li_3Sc_2(PO_4)_3$ were selected and electrochemically investigated with respect to their reduction stability. For comparison, the electrolyte $Li_{1.5}Al_{0.5}Ti_{1.5}(PO_4)_3$ was also included in the studies. $Li_3Sc_2(PO_4)_3$ proved to be chemically and electrochemically very stable and might act as an anode protection material in combination with lithium metal.

Experimental Section

Powder preparation. Powders in the $Li_{1+x}M^{3+}{}_xZr_{2-x}(PO_4)_3$ system were synthesized by the solution-assisted solid-state reaction (SA-SSR) as described elsewhere.[29] Stoichiometric quantities of high-purity Li_2CO_3 (Alfa Aesar, 99%), Sc_2O_3 (Projector GmbH, 99.5%), and ZrO_2 (Saint-Gobain, 99.8%) were mixed in a quartz glass beaker using H_2O to obtain a homogeneous aqueous suspension. Additionally, a corresponding amount of $NH_4H_2PO_4$ (Merck KGaA, 99%) was added during stirring. The whole mixture was stirred overnight at 250 rpm and at 70 °C for the slow evaporation of H_2O. The homogenized mixture was first heated up to 100 °C and then the dried solid mixture was calcined in an oven at 900 °C for 5 hours to form an amorphous raw powder. The annealed powder was then manually ground in an agate mortar and finally milled in a grinding bowl with ethanol as the dispersing medium and with 5 mm ZrO_2 balls using a planetary ball mill (Pulverisette 7 premium line, Fritsch Germany) at 350 rpm for 5 hours before being subsequently dried at 70 °C for 6 h. The particle size distribution (PSD) of the dry milled powders was verified with a laser scattering particle size analyzer (Horiba LA-950 V2 with a 650 nm and a 405 nm laser source). The resulting data were analyzed applying the Mie theory.[30,31] The powders after ball milling have a similar agglomerate morphology. Furthermore, the PSDs of all powders are nearly identical with a mean particle size of about 1.1 μm. Therefore, any differences in the sintering process are not related to the different particle sizes of the pressed powders.

Thermal analysis. Differential thermal analysis/thermogravimetry (DTA/TG) was performed on the calcined powders up to 1600 °C in air with heating and cooling rates of 300 K/h using the simultaneous thermal analyzer STA449F1 Jupiter coupled with the mass spectrometer QMS 403C Aëolos from NETZSCH-Gerätebau GmbH. The dilatometry experiments were also carried out with a 402C dilatometer from NETZSCH-Gerätebau GmbH. During the measurements, the change in length of the pressed pellets was recorded until a shrinkage of 25% was reached.

Pellet sintering. The annealed and freshly milled powders were pressed into pellets at a pressure of about 150 MPa and freely sintered in Pt crucibles. The sintering temperatures were extracted from the shrinkage curves of the dilatometer measurements. After sintering, the experimental density was determined geometrically. The theoretical density was obtained from the X-ray diffraction refinement results. In addition, to improve the densification process, advanced sintering methods were used: firstly, a two-stage sintering approach and secondly the field-assisted sintering technique, also known as spark plasma sintering (FAST/SPS).[32] By applying mechanical pressure and fast Joule heating, FAST/SPS enables the sintering of dense ceramics at lower temperatures with much shorter dwell times than conventional free sintering. The samples were sintered in a HP D 5 FAST/SPS device (FCT Systeme). A graphite foil (SGL Carbon) with a thickness of 0.35 mm was wrapped around the internal tube surface (diameter of 12 mm) fully covering the internal wall of a metal mold composed of the molybdenum-based alloy TZM (Plansee SE).

Subsequently, 2 g of NaSICON powder was filled in and sandwiched between two disks punched from graphite foil. The graphite foil served to separate the powder sample from the pressing tools to improve heat transfer and to facilitate the removal of the sample from the mold. The sintering was performed at temperatures of 1200 °C, 1150 °C, and 1000 °C for the materials $Li_{1.2}Sc_{0.2}Zr_{1.8}(PO_4)_3$, $Li_{1.2}Y_{0.2}Zr_{1.8}(PO_4)_3$, and $Li_{1.2}Al_{0.2}Zr_{1.8}(PO_4)_3$, respectively. A uniaxial pressure of 50 MPa was applied with a dwell time of 0.167 h in a vacuum. The heating rate was 600 K/h and a slow cooling rate of 120 K/h was applied in order to obtain crack-free samples. After ejection of the samples, the graphite foil was polished off from all pellet surfaces using SiC sandpaper. All samples were then thermally treated in air in a chamber furnace at 900 °C for 4 h to restore oxygen stoichiometry and to remove carbon residues.

Chemical analysis. The stoichiometry of the powders was controlled before and after free sintering by inductively coupled plasma optical emission spectroscopy (ICP-OES) using a Thermo Scientific iCAP7600 spectrometer with optical scale and CID semiconductor detector, axial und radial reflection, and wavelengths between 166 nm and 847 nm. 50 mg of powder was mixed with 0.5 g of lithium borate in a platinum crucible and fired for one hour at 1000 °C in a muffle furnace. The liquefied material was dissolved in 30 mL HCl (5%). After dissolution, the sample solutions were transferred to sample vials containing 0.5 mL of HF and filled to a volume of 50 mL. This measurement was performed twice for each composition.

Crystallography and microstructural analysis. The purity of the sintered specimens was measured by X-ray diffraction (XRD) from $2\theta = 10°$ to 60° with a step size of 0.02° and a measurement time of 0.75 s. The measurements were recorded with a Bruker D4 Endeavor diffractometer using Cu K_α radiation. The Rietveld analysis refinements to determine the lattice parameters of the resulting compounds were performed using the TOPAS V4.2 computer software (Bruker AXS 2008, Karlsruhe, Germany).

The microstructures of the polished cross-sections of the sintered pellets were examined by scanning electron microscopy (SEM, Ultra55, Zeiss).

Electrochemical characterization. Both sides of the prepared dense pellets were dry-polished using SiC sandpaper up to 4000 grit. Blocking electrodes were sputter-coated with gold onto both fresh surfaces for 2 minutes (~30 nm) using a Cressington 108 coater. Electrochemical impedance spectroscopy (EIS) was performed at 25 °C in a climate chamber (VT 4002EMC, Vötsch Industrietechnik) using a BioLogic VMP-300 multichannel potentiostat. The fre-

quency was varied from 7 MHz to 1 Hz with an amplitude of 10 mV. Impedance spectra were fitted using the software Zview® (Scribner Associates Inc). The impedance data were fitted using the equivalent. The electrical properties of the samples are represented by a combination of a resistance (R) and a constant phase element (CPE). The impedance of CPE is given by Equation (1) with $n < 1.0$ and $\omega = 2\pi\nu$ as the angular frequency. The C_{CPE} is related to the capacitance C as written in Equation (2).[33]

$$Z_{CPE} = \frac{1}{C_{CPE}\,(j\omega)^n} \tag{1}$$

$$C = R\frac{1-n}{n}C_{CPE}^{1/n} \tag{2}$$

R represents the long-range ionic conduction in the sample, CPE represents the non-perfect capacity of the specimen, CPE_{el} describes the blocking electrode/electrolyte interface at low frequencies.

After fitting the impedance spectra, the resistance was obtained by extracting the lowest value of $-Z''$ as the total resistance R. The total conductivity σ_t of the samples was calculated from the values R, L, and A using Equation (3)

$$\sigma = \frac{L}{A\,R} \tag{3}$$

in which L and A represent the pellet thickness and electrode surface area of the specimen, respectively.

Cyclic voltammetry (CV) measurements were performed using the VMP-300 potentiostat combined with the climate chamber and operated in the potential range from 0 V to 2 V with a scanning speed of 1 mV s^{-1}. For CV measurements, a thin gold layer was deposited on one side of the pellets and a lithium metal foil was attached to the other side. The cell assembly and measurements were performed in an Ar-filled glovebox and then sealed by hot glue to avoid contamination from ambient air. The measurements were carried out in Swagelok cells.

X-ray photoelectron spectroscopy (XPS). Samples after CV measurement showing a black discoloration on the surface were analyzed by X-ray photoelectron spectroscopy (XPS). XPS characterization was performed using a PHI5000 Versa Probe II instrument with monochromatized Al-K_α radiation (1486.6 eV). Samples initially sealed into aluminum pouch bags for transfer purposes were opened in an Ar-filled glovebox ($H_2O < 0.1$ ppm and $O_2 < 0.1$ ppm) and attached to an electrically insulating sample holder. This sample holder was subsequently transferred into the XPS chamber via an airtight transfer vessel. A dual beam charge compensation was applied during the measurements. The analysis beam diameter was 200 μm and the analyzer pass energy was 23.5 eV. For the Li-contacted sample, Ar was sputtered onto the sample surface (2× 2 mm area) for depth profiling. The acceleration voltage was 1 kV for the first 6 minutes (3 + 3 minutes) and 2 kV for the following 16 minutes (8 + 8 minutes). Casa XPS software was used for the data analysis. A linear energy calibration was applied to each spectrum so that the hydrocarbon peak was positioned at 284.8 eV. For all spectra, a Shirley background subtraction and intensity normalization (divided by the maximum intensity value) was applied to facilitate a comparison between the samples. During the peak fitting, a Gaussian/Lorentzian peak shape GL(30) was used for all peaks.

Acknowledgements

Financial support from the German Federal Ministry of Education and Research (BMBF) within the project Festbatt-Oxide (03XP0173A) and Festbatt2-Oxide (13XP0434A) is gratefully acknowledged. The authors thank Dr. E. Dashjav for technical support in converting XRD parameters, Dr. D. Sebold for SEM investigations, Mr. V. Bader for thermal treatments, Mrs. M.-T. Gerhards for DTA/TG measurements, and Dr. T.-P. Mishra for FAST/SPS experiments. We also thank the colleagues at ZEA-3 of Forschungszentrum Jülich for carrying out the ICP-OES measurements. Open Access funding enabled and organized by Projekt DEAL.

Conflict of Interest

The authors declare no conflict of interest.

Keywords: cation substitution · ceramics · cyclic voltammetry · electrochemistry · impedance spectroscopy · ionic conductivity · Li solid electrolyte · NaSICON

[1] A. Rossbach, F. Tietz, S. Grieshammer, *J. Power Sources* **2018**, *391*, 1–9.
[2] M. Hou, F. Liang, K. Chen, Y. Dai, D. Xue, *J. Nanobiotechnol.* **2020**, *31*, 132003.
[3] R. DeWees, H. Wang, *ChemSusChem* **2019**, *12*, 3713–3725.
[4] H. Aono, E. Sugimoto, Y. Sadaoka, N. Imanaka, G. Adachi, *J. Electrochem. Soc.* **1990**, *137*, 1023–1027.
[5] B. Kumar, D. Thomas, J. Kumar, *J. Electrochem. Soc.* **2009**, *156*, A506-A513.
[6] J. Fu, *Solid State Ionics* **1997**, *104*, 191–194.
[7] P. Hartmann, T. Leichtweiss, M. R. Busche, M. Schneider, M. Reich, J. Sann, P. Adelhelm, J. Janek, *J. Phys. Chem. C* **2013**, *117*, 21064–21074.
[8] W. D. Richards, L. J. Miara, Y. Wang, J. C. Kim, G. Ceder, *Chem. Mater.* **2016**, *28*, 266–273.
[9] Y. Liu, Q. Sun, Y. Zhao, B. Wang, P. Kaghazchi, K. R. Adair, R. Li, C. Zhang, J. Liu, L. Y. Kuo, *ACS Appl. Mater. Interfaces.* **2018**, *10*, 31240–31248.
[10] M. Catti, A. Comotti, S. Di Blas, *Chem. Mater.* **2003**, *15*, 1628–1632.
[11] S. Kumar, P. Balaya, *Solid State Ionics* **2016**, *296*, 1–6.
[12] C. R. Mariappan, P. Kumar, A. Kumar, S. Indris, H. Ehrenberg, G. V. Prakash, R. Jose, *Ceram. Int.* **2018**, *44*, 15509–15516.
[13] H. Xie, J. B. Goodenough, Y. Li, *J. Power Sources* **2011**, *196*, 7760–7762.
[14] K. Arbi, M. Ayadi-Trabelsi, J. Sanz, *J. Mater. Chem.* **2002**, *12*, 2985–2990.
[15] F. Zheng, M. Kotobuki, S. Song, M. O. Lai, L. Lu, *J. Power Sources* **2018**, *389*, 198–213.
[16] N. Anantharamulu, K. Koteswara, G. Rambabu, B. Vijaya, V. Radha, M. Vithal, *J. Mater. Sci.* **2011**, *46*, 2821–2837.
[17] H. El-Shinawi, A. Regoutz, D. J. Payne, E. J. Cussen, S. A. Corr, *J. Mater. Chem. A.* **2018**, *6*, 5296–5303.
[18] S. Smith, T. Thompson, J. Sakamoto, J. L. Allen, D. R. Baker, J. Wolfenstine, *Solid State Ionics* **2017**, *300*, 38–45.
[19] H. Xie, Y. Li, J. B. Goodenough, *RSC Adv.* **2011**, *1*, 1728–1731.
[20] A. Cassel, B. Fleutot, M. Courty, V. Viallet, M. Morcrette, *Solid State Ionics* **2017**, *309*, 63–70.
[21] Y. Li, M. Liu, K. Liu, C. A. Wang, *J. Power Sources* **2013**, *240*, 50–53.
[22] Y. Zhang, K. Chen, Y. Shen, L. Yuanhua, C. W. Nan, *Ceram. Int.* **2017**, *43*, S598-S602.
[23] T. Savitha, S. Selvasekarapandian, C. S. Ramya, *J. Solid State Electrochem.* **2008**, *12*, 857–860.
[24] T. Šalkus, A. Kežionis, V. Kazlauskienė, J. Miškinis, A. Dindune, Z. Kanepe, J. Ronis, A. F. Orliukas, *Mater. Sci. Eng. B* **2010**, *172*, 156–162.
[25] G. G. Amatucci, A. Safari, F. K. Shokoohi, B. J. Wilkens, *Solid State Ionics* **1993**, *60*, 357–365.
[26] T. Suzuki, K. Yoshida, K. Uematsu, T. Kodama, K. Toda, Z. G. Ye, M. Ohashi, M. Sato, *Solid State Ionics* **1997**, *104*, 27–33.

[27] T. Suzuki, K. Yoshida, K. Uematsu, T. Kodama, K. Toda, Z. G. Ye, M. Ohashi, M. Sato, *Solid State Ionics* **1998**, *113*, 89–96.
[28] M. Sato, T. Suzuki, K. Yoshida, K. Uematsu, K. Toda, Z. G. Ye, *J. Alloys Comp.* **1997**, *250*, 510–514.
[29] S. Naqash, Q. Ma, F. Tietz, O. Guillon, *Solid State Ionics* **2017**, *302*, 83–91.
[30] T. Wriedt, W. Hergert, Mie Theory: A Review, in Mie Theory, Vol. 169 of Springer Series in Optical Sciences, eds. W. Hergert, T. Wriedt, Springer, Berlin, Germany, **2012**, 53–71.
[31] J. A. Lock, G. Gouesbet, *J. Quant. Spectrosc. Radiat. Transfer* **2009**, *110*, 800–807.
[32] H. Zhu, J. Liu, *J. Power Sources* **2018**, *391*, 10–25.
[33] S. M. Haile, G. Staneff, K. H. Ryu, *J. Mater. Sci.* **2001**, *36*, 1149–1160.
[34] M. Catti, N. Morgante, R. M. Ibberson, *J. Solid State Chem.* **2000**, *152*, 340–347.
[35] W. Gebert, E. Tillmanns, *Acta Crystallogr. Sect. B* **1975**, *31*, 1768–1770.
[36] B. Wu, M. Zinkevich, F. Aldinger, D. Wen, L. Chen, *J. Solid State Chem.* **2007**, *180*, 3280–3287.
[37] Y. E. Gorbunova, V. V. Ilyukhin, V. G. Kuznetsov, A. V. Lavrov, S. A. Linde, *Dokl. Akad. Nauk SSSR* **1976**, *228*, 1329–1331.
[38] R. Murugan, V. Thangadurai, W. Weppner, *Angew. Chem. Int. Ed.* **2007**, *46*, 7778–7781; *Angew. Chem.* **2007**, *119*, 7925–7928.
[39] J. Wolfenstine, S. Smith, T. Thompson, J. Sakamoto, J. L. Allen, D. R. Baker, *Solid State Ionics* **2017**, *300*, 38–45.
[40] a) Q. Ma, C.-L. Tsai, X.-K. Wei, M. Heggen, F. Tietz, J. T. S. Irvine, *J. Mater. Chem. A* **2019**, *7*, 7766–7776; b) B. Davaasuren, F. Tietz, *Solid State Ionics* **2019**, *338*, 144–152.
[41] H. Aono, E. Sugimoto, Y. Sadaoka, N. Imanaka, G. Adachi, *Solid State Ionics* **1993**, *62*, 309–316.
[42] H. F. Peng, M. L. Gao, M. F. Wang, *Chin. J. Inorg. Chem.* **2011**, *27*, 1969–1974.
[43] D. Petit, P. H. Colomban, G. Collin, J. P. Boilot, *Mater. Res. Bull.* **1986**, *21*, 365–371.
[44] F. Sudreau, D. Petit, J. P. Boilot, *J. Solid State Chem.* **1989**, *83*, 78–90.
[45] H. El-Shinawi, C. Greaves, J. Janek, *RSC Adv.* **2015**, *5*, 17054–17059.
[46] V. Ramar, S. Kumar, S. R. Sivakkumar, P. Balaya, *Electrochim. Acta* **2018**, *271*, 120–126.
[47] A. B. Bykov, A. P. Chirkin, L. N. Demyanets, S. N. Doronin, E. A. Genkina, A. K. Ivanov-Shits, I. P. Kondratyuk, B. A. Maksimov, O. K. Mel'Nikov, L. N. Muradyan, *Solid State Ionics* **1990**, *38*, 31–52.
[48] S. E. Sigaryov, E. A. Genkina, B. A. Maximov, *Solid State Ionics* **1990**, *37*, 261–265.
[49] D. Rettenwander, A. Welzl, S. Pristat, F. Tietz, S. Taibl, G. J. Redhammer, J. Fleig, *J. Mater. Chem. A* **2016**, *4*, 1506–1513.
[50] I. A. Stenina, I. Y. Pinus, A. I. Rebrov, A. B. Yaroslavtsev, *Solid State Ionics* **2004**, *175*, 445–449.
[51] W. O. Milligan, D. F. Mullica, G. W. Beall, L. A. Boatner, *Inorg. Chim. Acta* **1982**, *60*, 39–43.
[52] O. S. Bondareva, M. A. Simonov, N. V. E. Belov, *Dokl. Akad. Nauk SSSR* **1978**, *240*, 75–77.
[53] D. W. J. Cruickshank, *Acta Crystallogr.* **1964**, *17*, 677–679.
[54] J. Joo, T. Yu, Y. W. Kim, H. M. Park, F. Wu, J. Z. Zhang, T. Hyeon, *J. Am. Chem. Soc.* **2003**, *125*, 6553–6557.
[55] H. Sowa, J. Macavei, H. Schultz, *Z. Krist.* **1990**, *192*, 119–136.
[56] P. Feng, M. Niu, C. Gao, S. Peng, C. Shuai, *Sci. Rep.* **2014**, *4*, 1–10.
[57] M. Mazaheri, A. Simchi, F. Golestani-Fard, *J. Eur. Ceram. Soc.* **2008**, *28*, 2933–2939.
[58] S. Naqash, F. Tietz, E. Yazhenskikh, M. Müller, O. Guillon, *Solid State Ionics* **2019**, *336*, 57–66.
[59] J. S. Lee, C. M. Chang, Y. I. Lee, J. H. Lee, S. H. Hong, *J. Am. Ceram. Soc.* **2004**, *87*, 305–307.
[60] R. D. Shannon, *Acta Crystallogr. Sect.* A **1976**, *32*, 751–767.
[61] K. Arbi, S. Mandal, J. M. Rojo, J. Sanz, *Chem. Mater.* **2002**, *14*, 1091–1097.
[62] K. Arbi, W. Bucheli, R. Jiménez, J. Sanz, *J. Eur. Ceram. Soc.* **2015**, *35*, 1477–1484.
[63] G. Ceder, S. P. Ong, Y. Wang, *MRS Bull.* **2018**, *43*, 746–751.
[64] Y. Xiao, Y. Wang, S. H. Bo, J. C. Kim, L. J. Miara, G. Ceder, *Nat. Rev. Mater.* **2020**, *5*, 105–126.
[65] Y. Zhu, X. He, Y. Mo, *ACS Appl. Mater. Interfaces* **2015**, *7*, 23685–23693.
[66] Y. Benabed, M. Rioux, S. Rousselot, G. Hautier, M. Dolle, *Front. Energy Res.* **2021**, *9*, 682008.
[67] C. Delmas, A. Nadiri, J. L. Soubeyroux, *Solid State Ionics* **1988**, *28–30*, 419–423.
[68] B. Lang, B. Ziebarth, C. Elsässer, *Chem. Mater.* **2015**, *27*, 5040–5048.
[69] X. Yao, B. Huang, J. Yin, G. Peng, Z. Huang, C. Gao, D. Liu, X. Xu, *Chin. Phys. B* **2016**, *25*, 018802.
[70] Y. Li, W. Zhou, X. Chen, X. Lü, Z. Cui, S. Xin, L. Xue, Q. Jia, J. B. Goodenough, *Proc. Nat. Acad. Sci.* **2016**, *113*, 13313–13317.
[71] Z. Bastl, A. Senkevich, I. Spirovova, V. Vrtilkova, *Surf. Interface Anal.* **2002**, *34*, 477–480.

Manuscript received: July 20, 2022
Revised manuscript received: August 25, 2022
Accepted manuscript online: August 29, 2022
Version of record online: September 15, 2022